

Received August 11, 2019, accepted August 28, 2019, date of publication September 2, 2019, date of current version September 16, 2019.

Digital Object Identifier 10.1109/ACCESS.2019.2939025

Power Line Extraction From Aerial Images Using Object-Based Markov Random Field With Anisotropic Weighted Penalty

LE ZHAO¹, XIANPEI WANG, HONGTAI YAO, MENG TIAN¹, (Member, IEEE), AND ZINI JIAN

Electronic Information School, Wuhan University, Wuhan 430072, China

Corresponding author: Xianpei Wang (xpwang@whu.edu.cn)

This work was supported by the National Natural Science Foundation of China under Grant 51707135.

ABSTRACT The extraction of power line plays a key role in power line inspection by Unmanned Aerial Vehicles (UAVs). While it is challenging to extract power lines in aerial images because of the weak targets and the complex background. In this paper, a novel power line extraction method is proposed. First of all, we create a line segment candidate pool which contains power line segments and large amount of other line segments. Secondly, we construct the irregular graph model with these line segments as nodes. Then a novel object-based Markov random field with anisotropic weighted penalty (OMRF-AWP) method is proposed. It defines a new neighborhood system based on the irregular graph model and builds a new potential function by considering the region angle information. With the OMRF-AWP method, we can distinguish between the power line segments and other line segments. Finally, an envelope-based piecewise fitting (EPF) method is proposed to fit the power lines. Experimental results show that the proposed method has good performance in multiple scenes with complex background.

INDEX TERMS Power line extraction, object-based Markov random field (OMRF), anisotropic weighted penalty, irregular graph model, potential function.

I. INTRODUCTION

Power line inspection is a basic and extremely important task for department of power grid [1], [2]. The power line inspection technology mainly includes five ways: manual inspection, helicopter inspection, robot inspection, satellite inspection and Unmanned Aerial Vehicles (UAVs) inspection [3]–[6]. In recent years, with the rapid development of UAVs technology, the feasibility of UAVs inspection has gradually increased. Compared with the first four methods, the low cost and high mobility of the UAVs inspection have great application potential [7].

Power line extraction is extremely important for UAVs inspection [8], [9]. First, it can help UAVs avoid hitting on power line which is important to ensure the flight safety of UAVs. Second, it is important for automated UAVs inspection because the ability to accurately extract power line is useful for guiding the UAVs flying along the line and automatically collecting data in power line corridors. Third, it is the basic

step for fault diagnosis of power lines, such as risk assessment of distance between the power line and adjacent tree. Therefore, power line extraction based on aerial image of UAVs has become a hot research issue. The sensors carried by the UAVs are different, and the datasets obtained are not same. For airborne LiDAR data and synthetic aperture radar (SAR) images, some methods have been proposed [10]–[12]. As for aerial images obtained by optical sensors, the researchers mainly face two major problems:(1) power lines are difficult to be extracted completely which caused by the weak targets of power lines; (2) power lines and other linear objects are difficult to be differentiated because of the complex background in aerial images. In order to solve the above two problems, the researchers have done some research work, and the current methods can be roughly divided into two categories: (1) power line extraction based on the features of line segments themselves; (2) power line extraction based on auxiliaries or context semantics.

For the former category, researchers mainly used the features of the power line itself, and took a prior knowledge as the criterion to extract power lines. For example,

The associate editor coordinating the review of this article and approving it for publication was Shovan Barma.

Tian *et al.* [13] used a kind of double-side filters to enhance the power lines and utilized the Hough transform (HT) to extract power lines. Song and Li [14] proposed a sequential local-to-global method based on matched filter (MF) and first-order derivative of Gaussian (FDOG) to extract power lines. Shuai *et al.* [15] adopted the ratio line detector to get the edge map and used HT to extract power lines. Yang *et al.* [16] utilized HT to extract line segments, and then the power line segments are extracted by the fuzzy C-means (FCM) clustering method. Yan *et al.* [17] first used a modified ratio line detector to get edge map and employed Radon transform to extract line segments, then used the group method and a Kalman filter to link and connect the segments into entire lines. Li *et al.* [9], [18] first utilized a Pulse Coupled Neural Filter (PCNF), and then used HT to extract line segments. Finally, K-means algorithm was used to distinguish between power lines and non-power lines. In addition to considering the basic line feature of the power line, these methods utilize the special features of the power line according to the subjective understanding of the aerial image scene, such as the particular length, width, orientation, or spectral characteristic, etc. These special features can be regarded as the prior knowledge and are often used as a direct criterion for distinguishing between power lines and non-power lines in the classification process. In general, the criterion for these methods to distinguish between the power line and non-power line in specific scenes is simple and straightforward, and the modeling process is relatively uncomplicated. However, they also have a common disadvantage. When the characteristics of the power line in the aerial image do not match the prior knowledge, the performance of the method may be significantly degraded. Unfortunately, this situation often occurs because that the complex background and lighting conditions of the power line corridor make it difficult to maintain consistent power line characteristics in aerial images.

For the latter category, researchers realized that the context information or auxiliaries embedded in the scene is a great source to supplement the inadequate features of power line. For example, Golightly and Jones [19] used pylon poles as auxiliaries in the line detection. Zhang *et al.* [20] used the spatial correlation between pylon and power line as the auxiliary information to extract power lines. Both in [19] and [20], pylon is used as an auxiliary object to assist the power line extraction. Liu *et al.* [21] proposed an improved randomized Hough transform (RHT) to extract power lines. Cao *et al.* [22] utilized Radon transform (RT) to extract power lines. Zhang *et al.* [23] used HT to extract line segments and utilized K-means in the Hough space to extract power lines. In [21], [22] and [23], power lines are regarded as parallel lines appearing in groups and they use this criterion as context-assisted information to extract power lines. Chen *et al.* [24] used a cluster Radon transform (CRT) to extract line segments and distinguish between power lines and other line segments based on the criterion that the background on both sides of power line is more similar. Shan *et al.* [8] proposed an automatic auxiliary selection and

TABLE 1. A summary of methods comparasion.

Method type	Author	Advantages and Limitations
Former category	Tian et al.,[13]	Advantages: Easy to model, the criteria are straightforward.
	Song et al.,[14]	Limitations: Low stability, the test image needs to match the prior condition.
	Shuai et al.,[15]	
	Yang et al.,[16]	
	Yan et al.,[17]	
Latter category	Li et al.,[9],[18]	
	Golightly et al.,[19]	Advantages: The information utilization in the image is higher, and the segmentation precision is higher.
	Zhang et al.,[20]	Limitations: Low stability in some scenes
	Liu et al.,[21]	
	Cao et al.,[22]	
	Zhang et al.,[23]	
	Chen et al.,[24]	
	Shan et al.,[8]	

context acquisition scheme to extract power lines. In [24] and [8], they set relatively fixed complex context information to extract power lines based on manual experience or a machine learning model. In the process of power line extraction, these methods not only use the local features of the power line itself, but also add some global features, such as features of auxiliary objects, parallel features between power lines, overall features of context semantics and so on. Combining these two features can not only make preliminary judgments from local information, but also make global judgments from a macroscopic perspective, which improves the accuracy of the method for power line extraction. Therefore, these methods of integrating local features and global features have better robustness and anti-noise ability when the auxiliary object exists or the set context semantic information is match the scene of the image. Unfortunately, these relatively ideal settings often do not match the realities. For example, although the power lines always co-occur with some auxiliary objects such as cable pylons, whether these auxiliary objects exist in the aerial image depends on the flying height of the UAVs and the shooting angle of camera. The background on both sides of power line may be obviously different due to the extremely complex background. We can regard the similarity between the test images and specific context information or the necessity of the existence of the auxiliary as a kind of prior knowledge. When the prior knowledge does not match the test images, the inappropriate global features will be counterproductive to the accuracy of method. Therefore, these methods also have their own specific application scenes.

A summary of the advantages and limitations of the above methods is shown in Table 1. For the above two categories of methods, a certain prior knowledge modeling is required. But the environment of the power line corridor is complex and varied, the more prior knowledge is used, the robustness of the method is difficult to guarantee. In essence, power line extraction is a process of segmenting a region with a specific similar feature from an image, which can be regarded as the problem of image segmentation. There are many methods to solve the image segmentation problem and they can be roughly divided into two categories: the basic segmentation

method and the semantic segmentation method [25]. The former category mainly includes watershed segmentation [26], [27], mean shift [28], super-pixel segmentation [29], [30]; The latter category mainly includes active contours [31], [32], the Bayesian network [33], the Markov random field model (MRF) [34]–[36]. The basic segmentation only performs simple over-segmentation on the image, and the result is a large amount of small blocks which are non-intersecting and adjacent. Each region has no specific meaning. The semantic segmentation is based on the observation information of the image, and each area of the result has a specific meaning. MRF is an undirected graph structure, it can well describe the spatial neighborhood relationship between elements and get relatively complete context information. Moreover, MRF is a method based on probability and statistics, which can better match the data characteristics of the image and integrate multiple features into the model. So that the process of segmentation can be unsupervised. Motived by this, we propose a novel power line extraction method based on MRF model. The basic process of our method is as follows. Firstly, we create a line segment candidate pool, which contains line segments as many as possible. Secondly, we construct an irregular graph model with these line segments as nodes. Then we define the new neiborhood system based on the irregular graph model and build a new potential function. By considering the multiple features of the line segments and the new potential function based on the new neighborhood relationship, the line segments in the pool are classified and the power line segments class is obtained. Finally, the power line segments are grouped and connected into entire lines.

Our main contributions are as follows: (1) We map the power line segments originally defined in the rule grid to the irregular topology structure, and use the K-nearest neighbor idea to obtain the neighborhood system under this irregular graph model. This makes us not have to consider the interference of the background part in the classification process, so that the method could greatly reduce the amount of calculation and improve the running speed. (2) When we model the label field, we consider anisotropy, which due to angle differences based on classification results. So that the method can optimize classification results by angle difference between power lines and other line segments. By doing this, the method can make full use of regional information and spatial neighborhood relationships. After that, the object-based Markov random field with anisotropic weighted penalty (OMRF-AWP) method can be established by combining (1) and (2). (3) When grouping and connecting power line segments, we take the situation that the power lines have a slight curvature and a certain width into account, the envelope-based piecewise fitting (EPF) method is proposed to fit power lines completely and accurately as much as possible. Experimental results show that the proposed method can extract power lines from complex background accurately.

The remainder of the paper is structured as follows. In Section II, we briefly introduce the fundamental of Markov random field model. In Section III, our proposed methods for

power line extraction are described in detail. In Section IV, we present and discuss experimental results. In Section V, we conclude our work.

II. MARKOV RANDOM FIELD(MRF) MODEL

Markov random field (MRF) method uses the graph model to get the joint probability distribution of the image and the segmentation, which is often used to solve image segmentation problems. For an image I with size $M \times N$, we can define a graph model $G = (V, E)$ over I . $V = \{V_i | 1 < i < n\}$ is the site set, each site V_i denotes the node in the graph model, which can represent a pixel ($n = M \times N$) or an object(n is the number of regions generated by over-segmentation) in the original image I . $E = \{e_{ij} | 1 < i, j < n\}$ is the edge set, where e_{ij} can describe the spatial relationship between V_i and V_j :

$$e_{ij} = \begin{cases} 0 & \text{when } V_i \text{ and } V_j \text{ are not adjacent} \\ 1 & \text{when } V_i \text{ and } V_j \text{ are adjacent} \end{cases} \quad (1)$$

Based on graph model G , two sub-random fields, label field and feature field, can be constructed. Label field can record the category of each node and imply the neighborhood relationship between the nodes. It is denoted as $X = \{X_1, X_2, \dots, X_n\}$, each X_i in the set X is a random variable, which represents the segmentation class for the node V_i . Assuming that there are k different classes in the image, then the class set $\Lambda = \{1, 2, \dots, k\}$ can be defined, the r.v. X_i takes values from set Λ . The feature field is used to record the feature vector representing each node, which can be denoted as $Y = \{Y_1, Y_2, \dots, Y_n\}$, each Y_i represents the feature vector at node V_i . When the observed image I is given, Y has a unique implementation y . Therefore, the image segmentation problem is converted into the following probability problem:

$$\hat{x} = \arg \max_{x \in \Omega} P(X = x | Y = y) \quad (2)$$

Here, $\Omega = \{x | x = \{x_i | i : V_i \in V, x_i \in \Lambda\}\}$ is a collection of all implementations of the label field. According to the Bayesian formula:

$$\begin{aligned} \hat{x} &= \arg \max_{x \in \Omega} P(x | y) \\ &= \arg \max_{x \in \Omega} \frac{P(y|x) \cdot P(x)}{P(y)} \\ &= \arg \max_{x \in \Omega} P(y|x) \cdot P(x) \end{aligned} \quad (3)$$

where $P(y|x)$ is a likelihood function to model the feature field when the label is given, and $P(x)$ is a prior function to describe spatial relationships. Based on the above ideas, the image segmentation problem can be converted into a probabilistic modeling problem for the feature field and the label field.

A. THE FEATURE FIELD MODEL

In the probability modeling process of the feature field, Gaussian mixture model (GMM) is widely used due to its simplicity, easy implementation, low complexity and ability to describe natural image features effectively. The feature

vector of each random variable can be denoted as $Y_i = (Y_i^1, Y_i^2, \dots, Y_i^p)^T$, p is the dimension of the feature vector. In the GMM, there are two hypothesis: 1) the features of each node are independent of each other after a given segmentation result, 2) The feature of each node obey the Gaussian distribution of the corresponding class. The parameters of GMM are the set of mean feature vector of each class $\mu = \{\mu_1, \mu_2, \dots, \mu_k\}$ and the set of feature covariance matrix of each class $\Sigma = \{\Sigma_1, \Sigma_2, \dots, \Sigma_k\}$, where k is the number of segmentation classes. So $P(y|x)$ can be expressed as:

$$P(Y = y|X = x) = P(y|x) = \prod_{i=1}^n P(y_i|x_i) \quad (4)$$

$$\begin{aligned} P(y_i|x_i=h) &= \frac{1}{(2\pi)^{p/2} |\Sigma_h|^{1/2}} \\ &\times \exp[-\frac{1}{2}(y_i - \mu_h)^T \Sigma_h^{-1} (y_i - \mu_h)] \end{aligned} \quad (5)$$

where μ_h and Σ_h respectively denote the mean vector and covariance matrix of the features in the class h . For the estimation of μ_h and Σ_h , we can use the maximum likelihood estimation algorithm to estimate them.

$$\mu_h = \frac{1}{|\{i|x_i=h\}|} \sum_{\{i|x_i=h\}} y_i \quad (6)$$

$$\Sigma_h = \frac{1}{|\{i|x_i=h\}| - 1} \sum_{\{i|x_i=h\}} (y_i - \mu_h) \cdot (y_i - \mu_h)^T \quad (7)$$

B. THE LABEL FIELD MODEL

For the label field, we assume that it is a Markov random field which satisfies Markov property, as described in the following equation:

$$P(x_i|x_j, j : V_j \in V \& j \neq i) = P(x_i|x_j, j \in N_i) \quad (8)$$

where N_i represents the neighborhood of node V_i , we define $N_i = \{j | e_{ij} \neq 0\}$, and then the neighborhood system $NS = \{N_i | 1 \leq i \leq n\}$ is obtained. According to Hammersley-Clifford theorem, MRF with neighborhood system NS is equivalent to Gibbs random field, so the label field $P(x)$ model is converted into Gibbs model:

$$P(x) = \frac{1}{Z} \times \exp \left[-\frac{1}{T} \cdot U(x) \right] \quad (9)$$

In equation (9), $Z = \sum_{x \in \Omega} \exp \left[-\frac{1}{T} \cdot U(x) \right]$ is a normalized constant called the partition function and T is a temperature constant, which is generally taken as 1. $U(x)$ is the energy function defined as the sum of clique potential over all possible cliques C contained in the graph structure $G = (V, E)$.

$$U(x) = \sum_{c \in C} v_c(x) \quad (10)$$

where, c is set of single-site cliques, pair-site cliques or triple-site cliques, C is a set containing all c , and $v_c(x)$ is the clique potential function corresponding to the clique c .

For the clique potential, there are many modeling methods, including Ising model, Potts model, (Multi-level Logistic Model)MLL model, Quadtree model, etc. Among them, MLL model is widely used due to its simplicity.

C. MAX A POSTERIOR

Based on the probabilistic modeling results of the above two random fields, the optimal process for segmentation can be obtained by the maximum posterior probability distribution (MAP) criterion:

$$\begin{aligned} \hat{x} &= \arg \max_x P(Y = y, X = x) = \arg \max_x P(y|x) \cdot P(x) \\ &\approx \arg \max_x \prod_{i=1}^n P(y_i|x_i) P(x_i|x_j, j \in N_i) \\ &= \arg \min_x \sum_{i=1}^n \ln [P(y_i|x_i) P(x_i|x_j, j \in N_i)] \\ &= \arg \min_x \sum_{i=1}^n [\mathcal{E}(y_i|x_i) + \mathcal{E}(x_i|x_j, j \in N_i)] \end{aligned} \quad (11)$$

Here, $\mathcal{E}(y_i|x_i)$ denotes the energy of feature field for node V_i . $\mathcal{E}(x_i|x_j, j \in N_i)$ denotes the energy of label field for node V_i .

When the segmentation result is updated according to the MAP criterion, each iteration first has a prior probability, that is, in each iteration process, the segmentation result needs to be a prior segmentation. In the first iteration update, there is no information about the label field, and the implementation of the label field needs to be initialized, and the result is used as the a prior implementation of the first iteration. In the subsequent $(t+1)$ th iteration, the posterior result of the t th is iteratively updated as the a prior result of the $(t+1)$ th. There are many methods for the initialization of the label field, in which the K-means algorithm has low computational complexity and a fast convergence speed, so it is often used as an method to obtain the initial segmentation of the label field.

III. PROPOSED METHOD

In this section, our proposed method will be described specifically, but before this, we first briefly explain the flow of the method. The structure of the proposed method is illustrated in Fig.1. It mainly consists of three steps: (1) First, we utilize the line segment detector (LSD) method to extract line segments in the aerial image and create a line segment candidate pool. (2) Second, we regard the line segments as nodes to construct an irregular graph model and define a new neighborhood system based on the irregular graph model. After that, we proposed an object-based MRF with anisotropic weighted penalty (OMRF-AWP) method to extract power line segments from line segment candidate pool. (3) Finally, an envelope-based piecewise fitting (EPF) method is proposed to fit power lines. The details of each step are as follows.

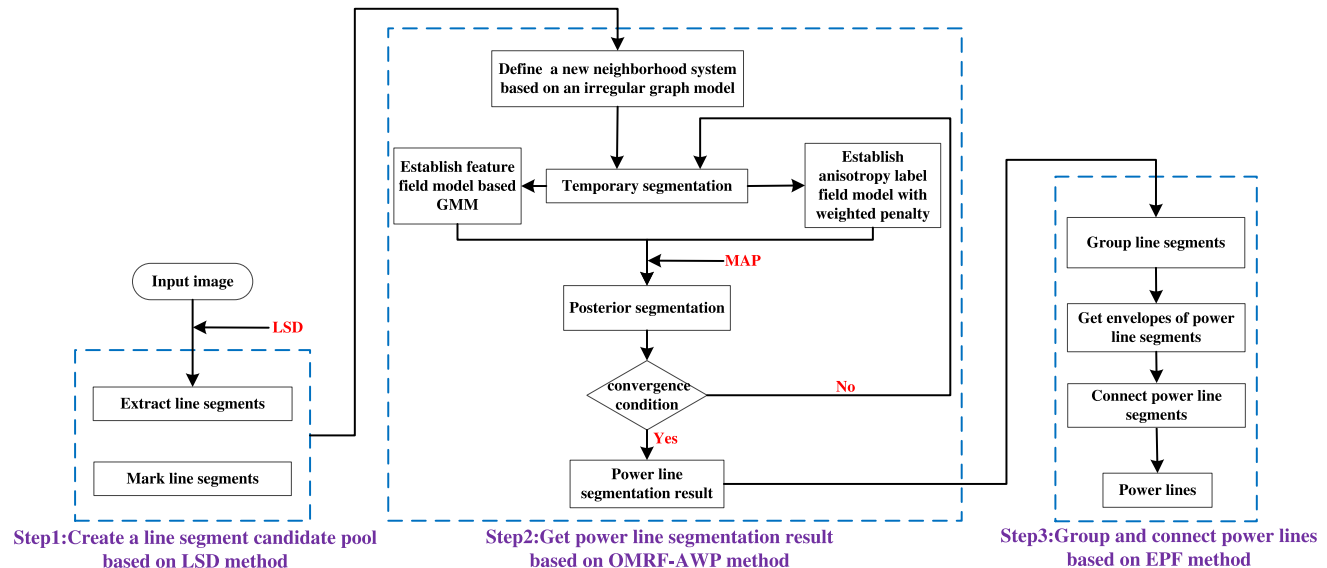


FIGURE 2. Original real aerial image.

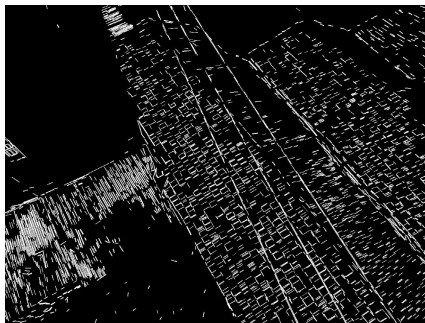


FIGURE 3. Result of line segments extraction by LSD method.

A. CREATE A LINE SEGMENT CANDIDATE POOL

In the process of creating the line segment candidate pool, we hope to be able to detect as many linear segments as possible, while not requires to differentiate power line segments from other line segments. Because the power line target is weak in the aerial image, it is unreasonable to use some filter at the step of line segments extraction to suppress the non-power line target. Because if some processing is

utilized to filter non-power lines, it is pretty possible to further weaken the strength of the power line signal.

There has been many methods for line segments extraction, such as Hough transform (HT) [37]–[39], Radon transform (RT) [40]–[42], line segment detector (LSD) [43]–[45] and so on. Among these methods, LSD method is widely used in recent years due to its fast computing speed, and no parameter adjustment required. Therefore, we utilize LSD method to extract line segments.

There is an original real aerial image captured from rural area by an UAV in Fig.2, and the extraction result of line segments is shown in Fig.3. Due to the extremely complex background, it is clearly that not only a large amount non-power line segments are extracted, but also the power lines are divided into many fragment regions. We define a site set $S^P = \{(s, t) | 1 \leq s \leq M, 1 \leq t \leq N\}$ for an image with size $M \times N$. Based on the result of LSD method, we can denote the edge map as set $R^L = \{r_{st} | (s, t) \in S^P\}$. r_{st} denotes the sequence number of the line segment region which contains the pixel at the position (s, t) in the image. Assume that there are n^l line segment regions in Fig.3, the variable r_{st} can take value from set $\Gamma = \{1, 2, \dots, n^l, \text{background}\}$. As shown in Fig.4, we can denote the line segment regions as set $L_i = \{(s, t) | r_{st} = i\} (1 \leq i \leq n^l)$ which named line segment candidate pool and denote the background region as set $B = \{(s, t) | r_{st} = \text{background}\}$.

B. EXTRACT POWER LINE SEGMENTS BASED ON OMRF-AWP METHOD

1) BUILD AN IRREGULAR GRAPH MODEL AND DEFINE THE NEW NEIGHBORHOOD SYSTEM

As shown in Fig.5, when we get the result of LSD method, the irregular graph model $G = (V, E)$ can be constructed

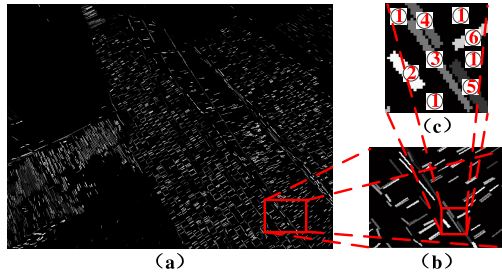


FIGURE 4. Mark each line segment region.

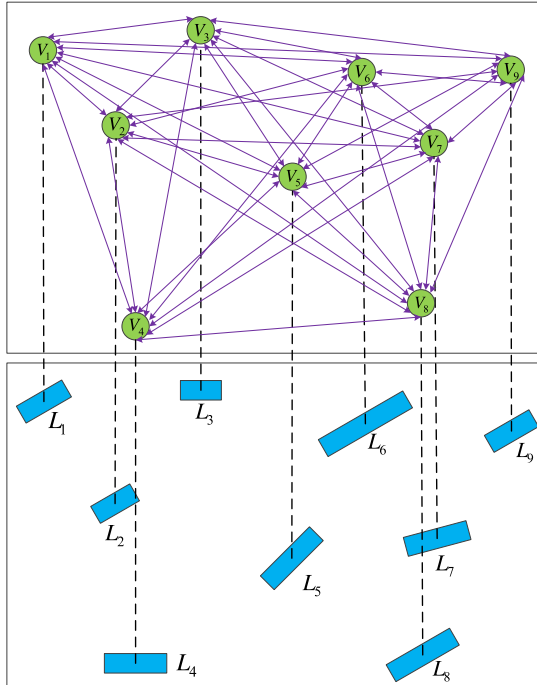


FIGURE 5. Irregular graph model based on line segment candidate pool.

based on the detected line segments. Where $V = \{V_i | 1 \leq i \leq n^l\}$, each V_i is a node which represents the line segment region L_i in the irregular graph model. The set $E = \{e_{ij} | 1 \leq i, j \leq n^l\}$ represents the adjacent degree between the nodes and e_{ij} denotes the the minimum Euclidean distance between line segment regions L_i and L_j . We can define the $d_{P_1 P_2}$ which represents the distance of any two pixels $P_1(s_1, t_1)$ and $P_2(s_2, t_2)$, and e_{ij} as following:

$$d_{P_1 P_2} = \sqrt{(s_1 - s_2)^2 + (t_1 - t_2)^2} \quad (12)$$

$$e_{ij} = \begin{cases} \min\{d_{P_1 P_2} | \forall P_1 \in L_i, \forall P_2 \in L_j\} & i \neq j \\ +\infty & i = j \end{cases} \quad (13)$$

After getting the irregular graph model, how to define the neighborhood system is one of the key problems. The definition of an object-based Markov random field neighborhood system is based on over-segmented regions, and they share boundaries with their neighbor regions. Also the definition of a pixel-based Markov random field neighborhood system is based on 4-connected regions or 8-connected regions in which the pixels are adjacent. But in this method, most of

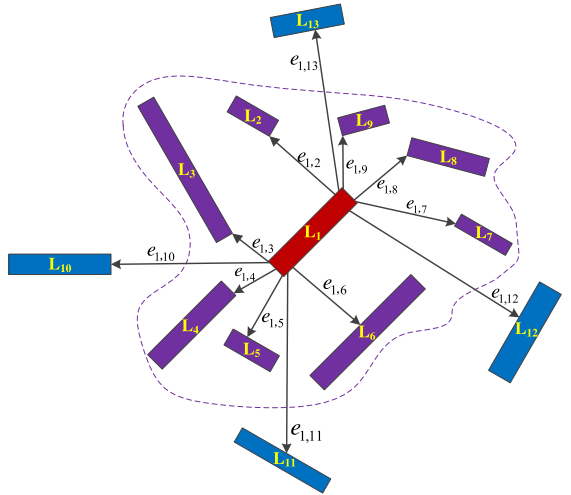


FIGURE 6. The defination of new neighborhood system based on irregular graph model.

the line segment regions are not adjacent directly, and some of them are even far apart from each other. Because of the non-direct adjacency, we employ the idea of K Nearest Neighbor (KNN) [46] to define the neighborhood system. For a certain line segment region L_i , its neighbor set N_i contains K line segment regions which are nearer than the other $n^l - K - 1$ line segment regions. Therefore, for this graph model, we give the definitions of neighbor set N_i and neighborhood system NS as following:

$$N_i = \{L_{i1}, L_{i2}, \dots, L_{iK}\} \quad (14)$$

$$NS = \{N_i | 1 \leq i \leq n^l\} \quad (15)$$

where L_{ik} represent a line segment region which is the K th nearest from L_i . In this paper, K take value of 8. For example, in the Fig.6, we assume that there are totally 11 line segment regions around line segment region L_1 , the neighbor set N_1 is consist of 8 line segment regions, $L_2, L_3, L_4, L_5, L_6, L_7, L_8$ and L_9 , which are nearer to L_1 than L_{10}, L_{11}, L_{12} and L_{13} .

The superiority of the irregular graph model and new neighborhood system mainly consist of two parts:(1) Based on the original graph model of MRF, it is inevitable to be interfered by background noise when extracting power lines from line segment candidate pool. However, based on the irregular graph model and neighborhood system, we do not have to consider the pixels in background region because they are not used in classification process. Therefore, it greatly improves the accuracy of power line extraction. (2) In the meantime, the efficiency is greatly improved because the number of pixels in background region which are ignored is pretty large.

2) DEFINE THE FEATURE FIELD MODEL

Based on the irregular graph model, we can define the feature field Y which consist of n^l line segment regions:

$$Y = \{Y_i | 1 \leq i \leq n^l\} \quad (16)$$

$$Y_i = \{y_{st} | (s, t) \in L_i\} \quad (17)$$

Here, y_{st} denotes the feature vector of site (s, t) in L_i . After the definition of feature field Y , the key problem is how to select features. First of all, we consider spectral features because it is the most basic feature of optical image and often used for image segmentation. The material of power line is more special than other objects, and the spectral characteristics of power line have a relatively consistency. In this paper, we transformed the original image from the RGB color space to HSI color space, then we used hue component H , saturation component S and intensity I as the first three components in the feature vector of each site. However, for the power line extraction problem, it is not enough to only use spectral information as a feature. Because the power lines in the aerial image tend to go through the whole image, the spectral feature of the different regions of the power line may not be exactly the same due to the influence of illumination. The power line can be regarded as a straight line in the aerial image captured by UAV (from overhead shot) and the size of the power line segment region in the line segment candidate pool is evenly distributed within a certain range because the width of the power line is consistent. Therefore, we used angle features and texture features as important auxiliary features to extract power lines. Angle features denote the angles of line segment regions or pixels in the background region. The texture feature can reflect the visual characteristics of homogenous phenomena in images and it is proportional to the size of the region. Then we can denote the form of feature vector y_{st} as:

$$y_{st} = (H_{st}, S_{st}, I_{st}, \alpha_{st}, \gamma_{st})^T \quad (18)$$

In equation (18), H_{st} , S_{st} and I_{st} denote the pixel spectral feature of a certain line segment region in line segment candidate pool, respectively. γ_{st} denotes the texture information of region to which the site (s, t) belongs. To define the texture information better, we introduce the concept of the information entropy [47]. The information entropy function can be denoted as $f(x) = x - x \cdot \log(x)$ and it is monotonously increased for $0 \leq x \leq 1$. The detail formula mode of γ_{st} are as follows:

$$\gamma_{st} = \frac{\kappa^{L_i}}{M \times N} \times (1 - \log(\frac{\kappa^{L_i}}{M \times N})), i : (s, t) \in L_i \quad (19)$$

Here, κ^{L_i} is the number of pixels in line segment region L_i to which the site (s, t) belongs. This component γ_{st} is an object-level feature.

As for the α_{st} , it denotes the angle of the line segment region L_i to which the site (s, t) belongs, so this component is an object-level feature, too. As shown in Fig.7, $P_1(s_1, t_1)$ and $P_2(s_2, t_2)$ are the two intersections of the centerline and the line segment region, so the α_{st} can be formulated as:

$$\alpha_{st} = \begin{cases} \arctan\left(\frac{t_1 - t_2}{s_1 - s_2}\right) & s_1 \neq s_2 \\ 90 & s_1 = s_2 \end{cases} \quad (20)$$

After that, we can get the likelihood function, which used to describe the feature field after a segmentation result is

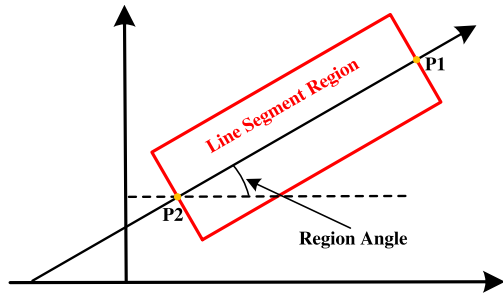


FIGURE 7. The defination for angle of line segment region.

given. The likelihood function can be denoted as equation (21) where $P(y_{st}|x_{st})$ can be calculated by equation (4)-(7).

$$\begin{aligned} P(Y = y|X = x) &= P(y|x) = P(y_1, y_2, \dots, y_{n'}|x) \\ &= \left[\prod_{i=1}^{n'} P(y_i|x_i) \right] \\ &= \left\{ \prod_{i=1}^{n'} \left[\prod_{(s,t) \in L_i} P(y_{st}|x_{st}) \right] \right\} \quad (21) \end{aligned}$$

3) DEFINE THE LABEL FIELD MODEL WITH ANISOTROPIC WEIGHTED PENALTY

For the label field, we utilized a novel method to construct the local probability model basd on the MLL model in this paper. Before introducing the novel method, we firstly recall the MLL model. Based on the graph model $G = (V, E)$ and neighborhood system N , we can denote the pair-site clique potential function $v_2(x)$ as the following:

$$v_2(x_i, x_j) = \begin{cases} -\beta & x_i = x_j \\ \beta & \text{otherwise} \end{cases} \quad (22)$$

Here, $L_j \in N_i$. Based on Equation (22), we can denote the local probability $P(x_i = k|x_{N_i})$ as:

$$P(x_i = k|x_{N_i}) = \frac{\exp[-\beta \cdot (8 - 2 \cdot n(x_i = k))]}{\sum_{k':k' \in \Lambda} \exp[-\beta \cdot (8 - 2 \cdot n(x_i = k'))]} \quad (23)$$

In equation (23), $n(x_i = k)$ denote the number of line segment regions in the neighbor set N_i whose segmentation label is equal to k . According to the equation (23), the local probability which using the isotropic can represent the neighborhood constraint relationship of the label field. For the current node, the number of its neighbor nodes are divided into a certain class is more, the local probability that the current node belongs to the class is greater. However, it is not suitable when the interaction between line segment regions is complex. We need not only to consider the existence of line segment regions in the graph model, but provide more context information of them to measure the strength of interaction as well. Therefore, we take the angle information with each pair-site clique into the irregular graph model and redefine

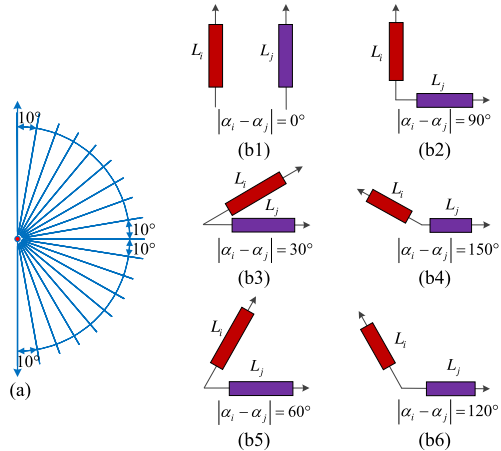


FIGURE 8. Construct the new MLL model with anisotropic weighted penalty.

the pair-site clique potential function, i.e.:

$$v'_2(x_i, x_j) = \begin{cases} -\beta \cdot \delta_{ij}(\Delta\alpha_{ij}) & x_i = x_j \\ \beta \cdot \delta_{ij}(\Delta\alpha_{ij}) & \text{otherwise} \end{cases} \quad (24)$$

$$\delta_{ij}(\Delta\alpha_{ij}) = \left| \left(\frac{\Delta\alpha_{ij}}{\lambda} - \frac{90}{\lambda} \right) \right| - \frac{45}{\lambda} \quad (25)$$

$$\Delta\alpha_{ij} = |\alpha_i - \alpha_j| \quad (26)$$

where $\delta_{ij}(\Delta\alpha_{ij})$ denotes the weight function between line segment regions L_i and L_j which can be used as a weighted penalty term to show the angle information between neighboring regions. λ denotes the weight coefficient. α_i and α_j denotes the angle of line segment regions L_i and L_j , respectively. $\Delta\alpha_{ij}$ denotes the absolute value of the angle difference between L_i and L_j whose range is $[0, 180]$. The weight function $\delta(\Delta\alpha)$ is monotonously decreased for $0 \leq \Delta\alpha \leq 90$. In the meantime, it is a symmetric function and the symmetry axis is $\Delta\alpha = 90$. Let $\beta_{ij} = v'_2(x_i, x_j)$ and we can denote the local probability $P'(x_i = k|x_{N_i})$ as:

$$P'(x_i = k|x_{N_i}) = \frac{\exp \left[- \sum_{j:L_j \in N_i} v'_2(x_i = k, x_j) \right]}{\sum_{k' \in \Lambda} \exp \left[- \sum_{j:L_j \in N_i} v'_2(x_i = k', x_j) \right]} = \frac{\exp \left[- \sum_{j:L_j \in N_i} \beta_{ij} \right]}{\sum_{k' \in \Lambda} \exp \left[- \sum_{j:L_j \in N_i} \beta'_{ij} \right]} \quad (27)$$

For the new MLL model, it considers the angle differences among the line segment regions in the local probability modeling and uses it as a weight to better reflect the constraint relationship between the neighborhoods. As shown in Fig.8(a), in this paper, we set $\lambda = 10$ and the value of the angle difference $\Delta\alpha$ is divided into 18 parts by 10 degrees. The Fig.8(b1)-Fig.8(b6) showed 6 different conditions in

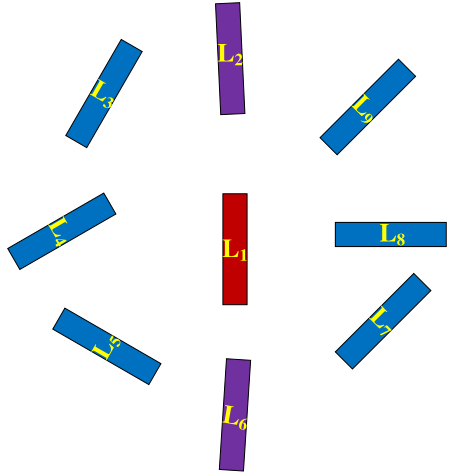


FIGURE 9. The example to explain the performance of the anisotropic MLL model with weighted penalty.

order to explain the property of redefined MLL model. In Fig.8(b1), line segment region L_j is parallel to line segment region L_i and the $\Delta\alpha_{ij} = 0$. The value of weight function $\delta_{ij}(\Delta\alpha_{ij})$ is largest at this condition. In the meantime, there is another extreme condition that L_i is vertical to L_j which is shown in Fig.8(b2). The $\Delta\alpha_{ij} = 90$ and the value of weight function $\delta_{ij}(\Delta\alpha_{ij})$ is smallest at this condition. The Fig.8(b3)-Fig.8(b6) aim to explain the symmetry. When we evaluate the parallelism of the two regions, if the angle between the two regions is an obtuse angle, then it can be converted to a complementary angle. Therefore, we can see that the higher the parallelism between the two regions for $0 \leq \Delta\alpha \leq 90$, the more possibility the two regions are classified into the same class. The main superiority of the redefined MLL model are discussed as follows. For example, we can see that, in the Fig.9, line segment regions $L_2, L_3, L_4, L_5, L_6, L_7, L_8$ and L_9 belong to the neighbor set of line segment region L_1 . L_1, L_2 and L_6 are power line segment regions, and all of other line segment regions are non-power lines. In the iteration, we assume that the L_2 and L_6 are divided into class 1 and the other line segment regions in the neighbor set of L_1 are divided into class 2. In this condition, the local probability that L_1 is classified into the class 2 is significantly higher than class 1 based on the original MLL model because the number of non-power line regions in the neighborhood set of L_1 is higher than the number of power line regions. However, the new MLL model has the potential to change this wrong case. Assume that $\Delta\alpha_{12} = 5, \Delta\alpha_{13} = 30, \Delta\alpha_{14} = 60, \Delta\alpha_{15} = 60, \Delta\alpha_{16} = 10, \Delta\alpha_{17} = 45, \Delta\alpha_{18} = 90$ and $\Delta\alpha_{19} = 45$, the local probability that L_1 is classified into the class 1 is higher than class 2 according the equation (24)-(27) which can help provide a more accurate power line extraction result.

4) MAX A POSTERIOR

After that, we can complete the modeling of two random fields, label fields and feature fields. In the process of

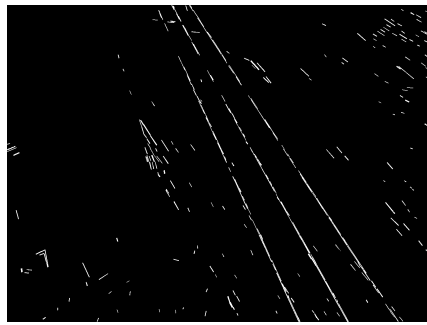


FIGURE 10. The classification result of power lines based on OMRF-AWP method.

updating the label field by using the MAP criterion, there is no information of the label field in the first iteration, so the label field needs to be initialized. In this paper, we choose the K-means algorithm which is used by most researchers as an implementation method of initialization. In the subsequent iteration, the t th post-test result is used as the $(t+1)$ th a prior hypothesis. The segmentation result \hat{x} can be obtained by the maximum posterior probability(MAP) distribution criterion, i.e.:

$$\begin{aligned}
 \hat{x} &= \arg \max_x P(Y = y, X = x) \\
 &= \arg \max_x P(y|x) \cdot P(x) \\
 &\approx \arg \max_x \prod_{i=1}^{n^l} P(y_i|x_i) P(x_i|x_j, j \in N_i) \\
 &= \arg \max_x \prod_{i=1}^{n^l} \left(\prod_{(s,t) \in L_i} P(y_{st}|x_i) \right) P(x_i|x_j, j \in N_i) \\
 &= \arg \min_x \sum_{i=1}^{n^l} \ln \left[\left(\prod_{(s,t) \in L_i} P(y_{st}|x_i) \right) P(x_i|x_j, j \in N_i) \right] \\
 &= \arg \min_x \sum_{i=1}^{n^l} \left\{ \left[\sum_{(s,t) \in L_i} \ln P(y_{st}|x_i) \right] \right. \\
 &\quad \left. + \ln P(x_i|x_j, j \in N_i) \right\} \\
 &= \arg \min_x \sum_{i=1}^{n^l} \left\{ \left[\sum_{(s,t) \in L_i} \mathcal{E}(y_{st}|x_i) \right] \right. \\
 &\quad \left. + \mathcal{E}(x_i|x_j, j \in N_i) \right\} \\
 &= \arg \min_x \sum_{i=1}^{n^l} [\mathcal{E}(y_i|x_i) + \mathcal{E}(x_i|x_j, j \in N_i)] \quad (28)
 \end{aligned}$$

We can obtain the power line classification result which is shown in Fig.10. The power lines are consist of several line segment regions and there are also a few line segments that are not power lines segmented into the power line class. Therefore, we need to further process the result of the OMRF-AWP method to obtain accurate and complete power lines. The details are as follows.

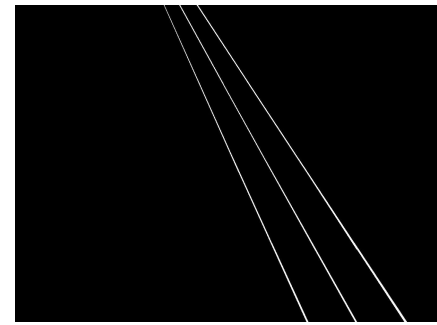


FIGURE 11. The final extraction result of power lines.

C. GROUP AND CONNECT POWER LINES

In this section, an envelope-based piecewise fitting (EPF) method is proposed which mainly consist of two parts: (1) Grouping line segment regions and filter out non-power line segment regions (2) Connect power line segment regions and extract power line pixels. The experimental result is shown in Fig.11.

For part (1), we utilize a line segment regions cluster method. The method flow is as follows:

(i) Based on the power line segmentation result, we can obtain the 4-connected region set $R^C = \{R_i^C | 1 \leq i \leq n'\}$. Here, n' is the number of 4-connected regions and $R_i^C \cap R_j^C = \emptyset (1 \leq i, j \leq n', i \neq j)$.

(ii) We can get the centroid of each region in R' by the way of finding the average value of regional coordinates. And we get the fitted line of each region in R' based on the method of least squares. The centroid set can be denoted as $P^C = \{P_1^C, P_2^C, \dots, P_{n'}^C\}$ and the fitted line set can be denoted as $L^C = \{L_1^C, L_2^C, \dots, L_{n'}^C\}$.

(iii) Set $t' = 1$ and distance threshold d_t .

(iv) We select one of ungrouped region R_i^C from set R^C as the seed region and save R_i^C in set $R_{t'}^{\text{temp}}$. We calculate the distance d_{ij}^C from the centroid P_j^C of any other ungrouped region R_j^C in set R^C to the fitted line L_i^C . If $d_{ij}^C < d_t$, we save R_j^C in set $R_{t'}^{\text{temp}}$ and update the slope and intercept of fitted line L_i^C based on all pixels in set $R_{t'}^{\text{temp}}$.

(v) Loop through step (iv) until all regions which can be saved in set $R_{t'}^{\text{temp}}$ are selected. Remove all regions in set $R_{t'}^{\text{temp}}$ from set R^C .

(vi) If $R^C = \emptyset$, we can get the set $R^{\text{TEMP}} = \{R_i^{\text{temp}} | 1 \leq i \leq t'\}$; else, set $t' = t' + 1$ and go to the step (iv).

(vii) Set the thresholds s_t , l_t and power line segment region R^P . We calculate the pixel number s_i^{temp} of region R_i^{temp} and the maximum value of the Euclidean distance l_i^{temp} between the any two pixels in region R_i^{temp} ($R_i^{\text{temp}} \in R^{\text{TEMP}}$). If $s_t \leq s_i^{\text{temp}}$ and $l_t \leq l_i^{\text{temp}}$, we can save R_i^{temp} into R^P . Finally, we can get the power line segment region set $R^P = \{R_m^P | s_t \leq s_m^P, l_t \leq l_m^P, 1 \leq m \leq \text{num}\}$. num is the number of selected sets from R^{TEMP} .

For part (2), it is the problem to connect power line segment regions in R^P . Although a single power line in the aerial image

captured by the UAVs(from overhead shot) can be regard as a straight line approximtely, the power line still has a slight curvature unless the shot angle of camera is perpendicular to the power line. When we use a single straight line equation to fit the power line, the extraction result will partially deviates from the real power line position. While if we denote each power line in a piecewise straight line, it will improve the extraction accuracy because the curvature of power line is small. Therefore, we propose a power line piecewise connect method in pixel level based on upper and lower envelopes in part (2). The method flow is as follows:

(i) We can get the central fitted line L_m^P of power line region R_m^P ($R_m^P \in R^P$) based on the method of least squares. $P_m^L(s_m^L, t_m^L)$ and $P_m^R(s_m^R, t_m^R)$ are the two intersections of the L_m^P and the edge of the image which can be calculated because that power lines cross the whole image. The maximum value ρ_m of the projection length of the power line between the image horizontal and vertical directions can be denote as $\rho_m = \max\{|s_m^R - s_m^L|, |t_m^R - t_m^L|\}$.

(ii) The envelope of R_m^P consist of two lines which can be defined as upper envelope line L_m^U and lower envelope line L_m^D . Each envelope line is divided into ω parts and the each interval length is ρ_m/ω . If ρ_m denotes the projection length of the power line in the horizontal direction, we can define the interval domain set D_m of envelope line as $D_m = \bigcup_{j=1}^{\omega} d_j$. Here, each interval d_j can be denoted as $d_j = [s_m^L + (j-1) * (\rho_m/\omega), s_m^L + j * (\rho_m/\omega)]$ ($s_m^L \leq s_m^R$). After that, we can define the upper and lower envelope line piecewise functions as $F_m^U(s)$, $F_m^D(s)$, i.e.:

$$F_m^U(s) = \sum_{j=1}^{\omega} \chi_{d_j}(s) f_j^U(s) \quad (29)$$

$$F_m^D(s) = \sum_{j=1}^{\omega} \chi_{d_j}(s) f_j^D(s) \quad (30)$$

$$\chi_{d_j}(s) = \begin{cases} 0 & s \notin d_j \\ 1 & s \in d_j \end{cases} \quad (31)$$

where, $f_j^U(s)$ and $f_j^D(s)$ are the envelope fitting function in the interval d_j .

(iii) In order to smooth the connection between piecewise functions as much as possible, a fitting algorithm with overlapping regions is proposed. Set interval overlap threshold ξ and define the set D'_m of domain with overlapping regions which is used to fit envelope. The set D'_m can be denoted as $D'_m = \bigcup_{j=1}^{\omega} d'_j$, where d'_j can be denoted in equation (32), i.e.:

$$d'_j = \begin{cases} [s_m^L, s_m^L + \rho_m/\omega + \xi] & j = 1 \\ [s_m^L + (j-1) * \rho_m/\omega - \xi/2, s_m^L + j * \rho_m/\omega + \xi/2] & 1 < j < \omega \\ [s_m^R - \rho_m/\omega - \xi, s_m^R] & j = \omega \end{cases} \quad (32)$$

(iv) We can get the upper and lower edge pixels of region R_m^P in d'_j . Then the $f_j^U(s)$ and $f_j^D(s)$ can be fitted based on the edge pixels with least square method. Therefore, we can get $F_m^U(s)$ and $F_m^D(s)$ based on D'_m .

(v) Based on $F_m^U(s)$ and $F_m^D(s)$, we can get the power line pixels between the upper and lower envelopes. Remove R_m^P from R^P .

(vi) Loop step (i)-(v) until $R^P = \emptyset$.

The all flow of our proposed method is as follows:

Algorithm 1

Require: image I , number of classes k , potential function parameter β

Ensure: the power lines segmentation;

- 1: Use LSD to get the line segment regions $V = \{V_i | 1 \leq i \leq n^l\}$, construct the irregular graph model $G = (V, E)$ and neighborhood system $NS = \{N_i | i = 1, \dots, n^l\}$;
- 2: Utilize the classical K-means algorithm to segment these regions to k classes, get the pixel-level segmentation, and denote the result as x^P . Initial the prior information $x(0) = \{x_i(0) | 1 \leq i \leq n^l\}$ of the label field X based on x^P ;
- 3: Set $t = 0$;
- 4: Estimate parameters $\mu(t)$ and $\Sigma(t)$ of the likelihood function $P(y_i|x_i(t+1), \mu(t), \Sigma(t))$ in (21) based on $x(t)$;
- 5: For label $x_i(t+1) \in \Lambda$ of each region L_i , calculate clique potential $v_2'(x_i(t+1), x_j(t))$ in (24) based on x_t , and get the joint Gibbs distribution $P'(x_i(t+1)|x_{N_i}(t))$ in (27).
- 6: Sequentially update each $x_i(t)$ into $\hat{x}_i(t+1)$ using the MAP in (28);
- 7: Renew the label field $x(t+1) = \{\hat{x}_i(t+1) | 1 \leq i \leq n^l\}$; If $x(t) \neq x(t+1)$, set $t = t + 1$ and go to step 4; else output $x(t+1)$.
- 8: Get the 4-connected regions $R^C = \{R_i^C | 1 \leq i \leq n'\}$ based on $x(t+1)$, group the regions in R^C and filter out non-power line segment regions, then get $R^P = \{R_m^P | s_t \leq s_m^P, l_t \leq l_m^P, 1 \leq m \leq num\}$;
- 9: Get $F_m^U(s)$ and $F_m^D(s)$ of region R_m^P in R^P , then we can obtain the power line pixels between $F_m^U(s)$ and $F_m^D(s)$.
- 10: Loop step 9 until all the regions in R^P are processed. Finally, we can extract power lines in pixel level.

IV. EXPERIMENTAL RESULT

In this paper, the dataset includes 134 images with size 1600×1200 which are taken by a DJ Phantom 4 UAV over Wuhan rural areas in October, 2016 and April, 2017. Based on the dataset, two seperated experiments are designed and implemented by a PC with a core i5-6500 CPU 3.2-GHz with 8-GB memory. In section IV-A, we classify the collected images according to image complexity and describe the relevant evaluation indicators. In section IV-B, we focus on how to take values for the two important parameters involved in OMRF-AWP method, and analyze the influence of different parameter values on experimental results. In section IV-C, we compare the performance of the proposed method in this paper with several classical methods. The details are as follows:

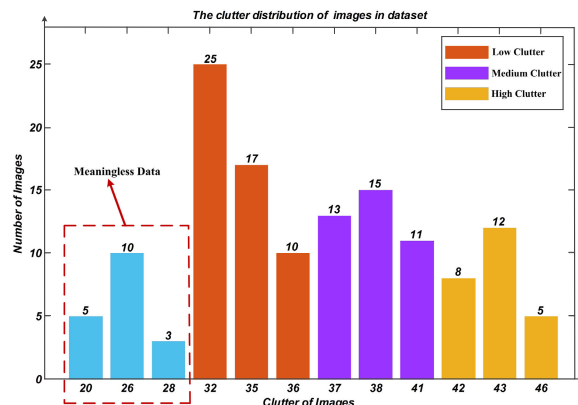


FIGURE 12. The image clutter statistics of images in the dataset.

A. MATERIALS

Image clutter (IC) is a common index used to judge the background complexity of an image [14], [48]. For an image I with a resolution of $M \times N$, the IC is as follows:

$$IC = \sqrt{\frac{1}{K} \sum_{i=1}^K \sigma_i^2} \quad (33)$$

where K is the number of sub-windows that the image are divided into. In this paper, K is set according to references [14] and [48]. σ_i^2 is the variance of the intensity of pixels in i -th sub-window which can be obtained by equations (34) and (35), i.e.:

$$\mu_i = \frac{1}{N_i} \sum_{j=1}^{N_i} (X_j) \quad (34)$$

$$\sigma_i = \sqrt{\frac{1}{N_i} \sum_{j=1}^{N_i} (X_j - \mu_i)^2} \quad (35)$$

In the equation (35), μ_i is the intensity mean of the pixels in the i -th sub-window and N_i is the pixel number of i -th sub-window.

As shown in Fig.12, the index IC distribution of the images in the dataset takes values in the interval [20], [46], and the mean cluster of images is 35.7. In the dataset, the background of the images which image clutter belongs to the interval [20], [28] is mainly consist of the sky with high gray level consistency. We define these images as meaningless data and discard these images because of their simple background. In order to test the impact of different image clutter on the proposed method, we divide the images in the dataset into three classes and performed power line extraction experiments. We define images with IC in the interval [32], [36] as low clutter data, images with IC in the interval [37], [41] as medium clutter data and images with IC in the interval [42], [46] as high clutter data. The percentage of the three types of clutter level is 38.8%, 29.1% and 18.7%, respectively.

In this paper, we use true positive rate(TPR) and false positive rate(FPR) to judge the performance of the methods for extracting power lines in pixel-level. The TPR and FPR can be denoted as equation(36)-(37), i.e.:

$$TPR = \frac{TP}{TP + FN} \quad (36)$$

$$FPR = \frac{FP}{FP + TN} \quad (37)$$

Here, TP is true positive number of correct detected power line pixels and FP is false positive number of mistaken detected power line pixels. TN is true negative number of correct detected non-power line pixels and FN is false negative number of mistaken detected non-power line pixels. Obviously, High TPR means that the power lines are extracted relatively complete. Low FPR means that few non-power lines are misclassified into power line class. Specially, the all true positive power line pixels in the image are labeled manually.

B. PARAMETERS DISCUSSION

In this section, we mainly discuss the influence of parameters setting in OMRF-AWP method on the power line classification results. There are two important parameters in OMRF-AWP method: number of classes of image classification semantics k and the Gibbs potential function parameter β .

In the classical Markov random field, the number of classifications is generally set by the semantics of the features in the actual image and the classification requirements. Only β , the parameter of the potential energy function, has an effect on the final classification result. For example, for an image made up of forests, towns, rivers and farmland, we can roughly set the parameter $k = 4$ and then explore the best value range for parameter β . However, the above way of parameter setting is not applied to the OMRF-AWP method, because it is difficult to obtain the number of line segment regions classes by simple visual observation. Forests, towns, rivers and farmland often have a certain area in the image, and the spectral features are easy to distinguish manually. But the number of line segments in line segment candidate pool is large, and it is difficult to distinguish them according to spectral features. For the OMRF-AWP method, each image has its own appropriate, optimal number of classifications. When the number of classifications is smaller than the optimal number of classifications, the method will classify the different classes together, resulting in a large number of misclassifications, which will eventually have an adverse effect on the power line fitting results. If the number of classifications is larger than the optimal number of classifications, the power lines belonging to the same class may be divided into multiple classes, so that the extracted power lines are disordered and the process of power line fitting cannot be performed. In order to determine the optimal number of classification k , we choose the IC as the reference parameter. IC can be used as the important evaluation indicator to characterize the degree of image gray level diversification. When the

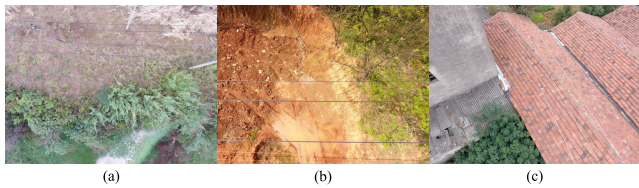


FIGURE 13. Three images of different *IC*.

image clutter is high, it indicates that the intensity differences between pixels in the image is large, and the probability of gradient in each direction is high. In other words, the probability of existing more line segments in each direction in the line segments candidate pool which obtained from this image is high. On the contrast, the probability that the angles of the line segments are concentrated is relatively large when the image clutter is low. Based on the above analysis, we suspect that the optimal classification number can be obtained based on the *IC*. When the *IC* is high, the classification number k is also high; when the *IC* is low, the classification number k is also low.

In order to verify our speculation, we selected three images of different image clutter from the database and designed the experiments separately. As shown in Fig.13, the *IC* of (a), (b) and (c) are 32, 38 and 42, respectively. Parameter k takes values from the interval [2], [18] and parameter β takes values from the interval [1,100]. A total of 1700 experiments are performed for each image. In particular, the experiments designed in this section are used to verify the classification performance of OMRF-AWP method under different parameters, so the EPF method is not used. In the evaluation of the classification performance, the TPR and FPR are calculated by taking the pixels in line segment candidate pool as the sample population, rather than based on all the pixels of the entire image. Therefore, when we calculate TPR and FPR according to equations (36)-(37), each parameter, such as TP, FP, TN and FN, is only used for pixels in the line segment candidate pool, excluding pixels of the background region.

When the parameter k is given and the experimental results satisfy the following 3 conditions, we think k is the optimal classification class. The importance of the three judgments is reduced in the order listed below. (1) In the range of parameter β , most of the classification results have higher TPR. (2) In the range of parameter β , most of the classification results have lower FPR. (3) Both of the TPR and FPR have a small fluctuation range. Because high TPR and low FPR indicate that most of real power line pixels are divided into one class and few non-power line pixels are divided into the class. In particular, if the experimental results of multiple classification classes have high TPR, we prefer to choose the class with the highest TPR as the optimal candidate class. Meanwhile, when the experimental results of this classification class have a relatively small FPR, we consider this class to be optimal even though the FPR are not smallest. Because we can use the EPF method to further filter out the noises, so the FPR can

be further reduced. However, if the TPR of the power line classification result is not high enough, this may eventually lead to an inability to fit the power line accurately. At the same time, the difficulty of selecting the parameter β can be significantly reduced when the third condition is satisfied.

We have discussed the optimal parameters k of the three images of different *IC* based on the above three criterions. There are a total of 1700 sets experimental result for each image and it is difficult to distinguish the best classification class. Fortunately, mean and standard variance can reflect the distribution of a sample set and they are common tools for measuring statistical analysis. Therefore, we calculate the mean and standard variance of the 100 sets of data for each class. As shown in Fig.14(a1) and Fig.14(a2), we can find that when the parameter $k = 4$, the experimental results of the image of low *IC* are the best. Because when we set $k = 4$, the mean TPR of the experimental results is highest and although the mean FPR is not the smallest among all the experimental results, it does not exceed 25%, which is acceptable. Moreover, both of the variances of TPR and FPR are relative small which means small fluctuation in experimental results. Based on the same criteria, as shown in Fig.14(b1), (b2), (c1) and (c2), we can find that the experimental results of the image of medium *IC* are better when parameter $k = 6$, and the experimental results of the image of high *IC* are better when parameter $k = 9$. On the basis of the optimal class, if the number of classifications is too large, the power lines will be divided into different classes, and the obtained power lines are messy and disconnected. If the number of classifications is too small, there will be two cases: (1) the power line segments and other line segments are divided into one class which is not conducive to the subsequent line grouping process; (2) When there are a lot non-power line segments adjacent to the power lines, the power lines will be divided into other classes, and finally there is no separate power line class. The experimental results show that when the *IC* level increases, the optimal parameter k increases, which confirms our previous speculation.

For the proposed OMRF-AWP method, in addition to the parameter k , special attention needs to be paid to the influence of the parameter β on the experimental results. With respect to (a) to (c) of Fig.13, as described above, after the optimal k is given, β takes different values, and different power line segments classification results are also obtained. For images with low *IC*, as shown in Fig.15(a1), when the β increases, the TPR rises first and then fall down, after that the TPR rises again, finally falls to a steady state. We name the state of the first rise and fall of the TPR as the coaction state of the label field and the feature field. In this state, the energy of the label field gradually increases, and the line segments with smaller angle differences around the power line segments are gradually divided into one class. However, when the energy of the label field is getting closer to the energy of the feature field, the power line segments with similar features but large angle differences are possibility divided into different classes. Therefore, in the coaction state,

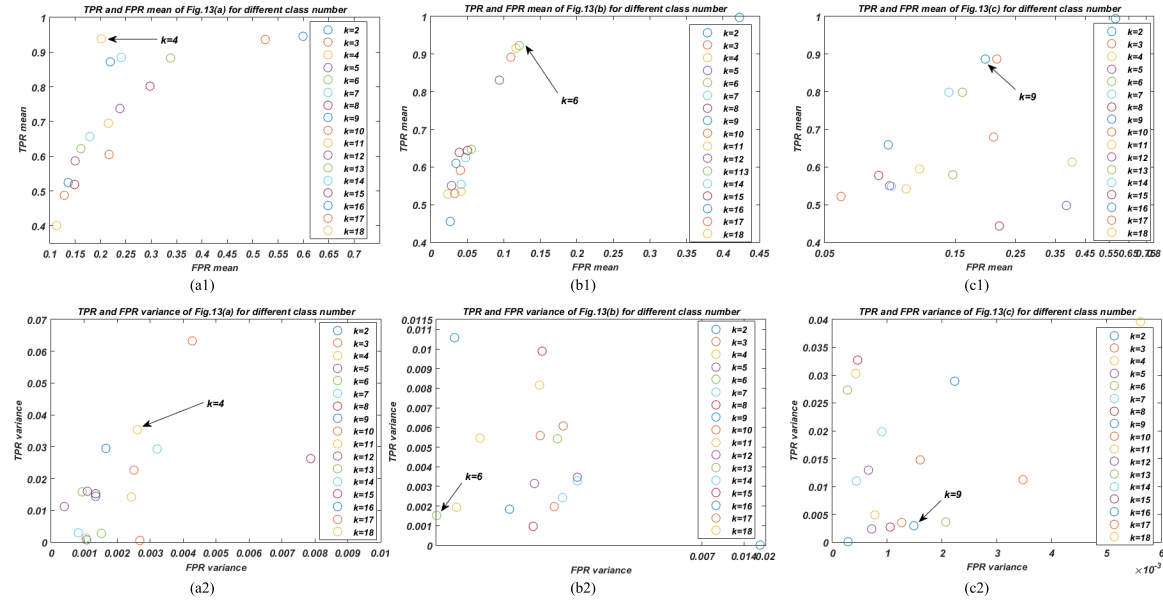


FIGURE 14. The experimental results of exploring the optimal class. (a1)(b1)(c1): mean of TPR and FPR for different class number; (a2) (b2) (c2): variance of TPR and FPR for different class number.

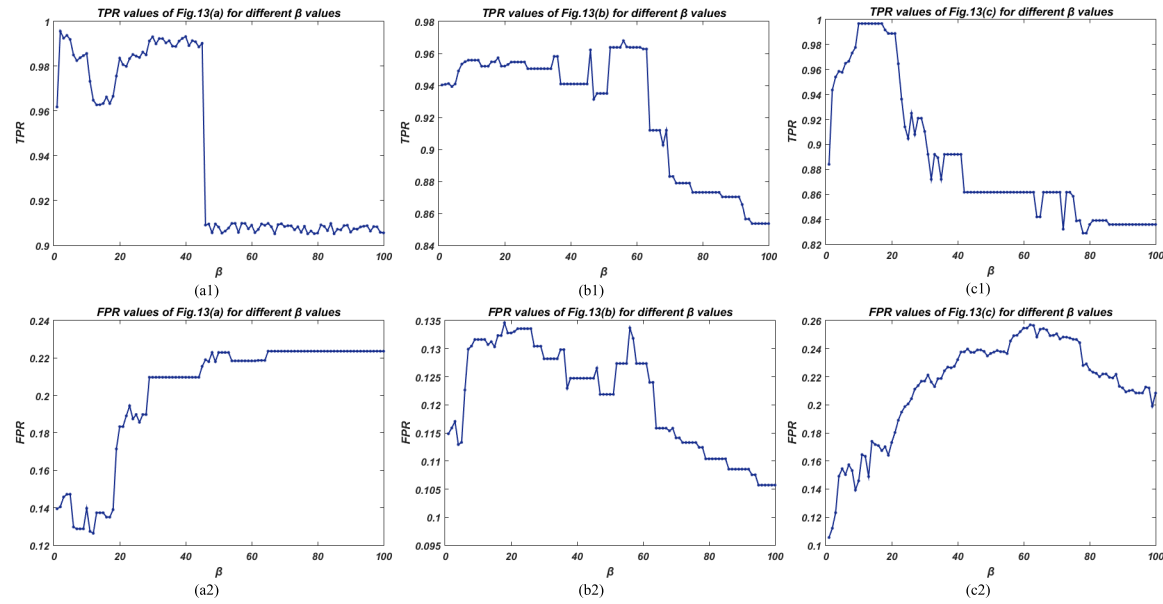


FIGURE 15. The variation of TPR and FPR of the three images. (a1)(a2): TPR and FPR of Fig.13(a) for different β ; (b1)(b2): TPR and FPR of Fig.13(b) for different β ; (c1)(c2): TPR and FPR of Fig.13(c) for different β .

the TPR rises first and then falls. The state of the second rise and fall of the TPR can be regarded as the separate action state of the label field. Due to the small spectral fluctuation of the image of low IC , the energy of the feature field which mainly composed of the spectral features is relatively small. In this state, as the β increases, the magnitude of the label field energy gradually exceeds the magnitude of the feature field energy. So in addition to the role of the feature field during the initial classification process, the label field is changing

the label of each element in the subsequent classification iteration process. When β increases, power line segments with inconsistent spectral features but similar angles are gradually divided to the power line classes. However, when the value of β exceed a certain threshold, the label field work independently on the classification result because its energy is much larger than the energy of the feature field. It is inevitable that some power lines and non-power lines are divided into one class. Because in this condition, whether different line

segments can be divided into one class will only depend on the labels and the angle differences of their neighborhood line segment regions based on the anisotropic MLL model. Therefore, the TPR rises first and then falls. When the β is high enough, the classification result no longer changes, and the TPR tends to be stable. As shown Fig.15(b1) and Fig.15(c1), we find that the TPR of medium IC and high IC images are only one rise and fall process. Because medium IC and high IC images have large feature field energy due to the large spectral features fluctuations, so in the gradual increase of β , the feature field can always contribute to the classification result. Therefore, for images with medium and high IC values, as the parameter β increases, the classification result obtained by our proposed OMRF-AWP method, TPR only shows the first change phase of the low IC image.

As shown in Fig.15(a2), (b2) and (c2), for the image with low IC , when β changes from 1 to 100, the FPR rises first and fall down, then rise until it reaches a steady state. For the images with medium and high IC , when β changes from 1 to 100, the FPR increases first and then decreases. Because for low IC , there are two stages in the classification process: coaction state and separate action state. In the coaction state, since only the features are considered in the initial classification process, the line segments which have similar features are divided into one class, and it is inevitable that some non-power line segments whose features are similar to the power lines are misclassified into power line class. When the β is small, it is not possible to separate these non-power lines from the power line class, but instead pull other non-line segments adjacent to these line segments with similar orientations into the power line class. However, when the β rises to a certain stage, the non-power lines that are misclassified into the power line class and whose angles are inconsistent with the adjacent power lines will be gradually separated from the power line class. Therefore, the FPR rises first and then falls. In the separate action state, the final classification result only depends on the role of the label field. The power line segments pull all the line segments with similar angles around them to the power line class until the non-power lines with similar angles around them are all divided into power line class. So the FPR rise again and then reaches a steady state. But for images with medium IC and higher IC , the feature field energy is large and will not be masked by the label field energy as the β increases. Therefore, their FPR rise first and then fall down in the coaction state.

C. METHODS COMPARISON

In order to further evaluate the performance of the proposed method, we compare it with the following five methods: (1) LSD-based object-level Markov random field (LSD-based OMRF method) [36], [43] (2) LSD-based pixel-level Markov random field(LSD-based pMRF method) [34], [43] (3) We name the method of reference [17] as AEPL method. (4) We name the method of reference [9] as TAPLD method. (5) We name the method of reference [24] as CRT

method. The work flows of AEPL, TAPLD and CRT are introduced in Section I.

For the method (1), in the initialization phase, the over-segmented region and the line segment region are combined to generate a new object region map. The line segment portion is divided into k classes, and other portions are used as background, which are self-contained, and the two are combined to obtain an initial classification. The tempory result is substituted into OMRF for iterative optimization. For the method (2), in the initialization phase, the line segment result extracted by the LSD is divided into k classes, and the other pixels are regarded as one class, and the two parts classification are combined as the classification results of the whole image to be iteratively optimized as the initial classification of the pMRF. The purpose for the comparison with method (1) and method (2) is to prove that the proposed method is valid for the improvement based on the traditional Markov random field. As for the methods (3), (4) and (5), they are classical methods for power line extraction in complex background. Therefore, the comparison with methods (3), (4) and (5) can prove the superiority of the proposed method in the field of power line extraction.

Besides the 3 images which used to dicuss the important parameters in the section IV-B, we randomly selected 2 images from the low IC sub-dataset, medium IC sub-dataset and high IC sub-dataset as experimental data, respectively. Therefore, a total of 9 images are used to test the performance of the six methods and the the experimental results of three sets of low IC images, medium IC images and high IC images are shown in Fig.16, Fig.17 and Fig.18, respectively.

In order to ensure the fairness of the comparison process as much as possible, we set the parameters of the six methods as follows: method (1), (2) and the proposed method are all based on MRF model, so the classification numbers k of the three methods are the same, and the method (1) and the proposed method are both object-level MRF, their β values are consistent with each other. Method (2) is based on pixel-level MRF, we set a β value as a fixed value of 0.5 which is the recognized effective value of the pMRF model. The parameters setting of Methods (3) and (5) have not been quantitatively discussed in detail in the references [17] and [24], so we try our best to ensure that the thresholds are optimal as much as possible according to the experimental results. For Method (4), according to reference [9], the linking strength is set to 0.2, the number of classifications of Kmeans is set to 4, and the number of iteration of PCNF is set to 3. Specailly, the line segments detected by Methods (3), (4) and (5) may not completely pass through the pixel points, and we optimize them as much as possible to improve the experimental results. In this section, we still choose TPR and FPR as indicators to measure the performance of the five methods, but the calculation process is different from the section IV-B. In this section, we use the entire image as the sample population instead of the line segment region detected by the LSD as the sample population. Therefore, the values of parameters TP, FP, TN and FN are calculated

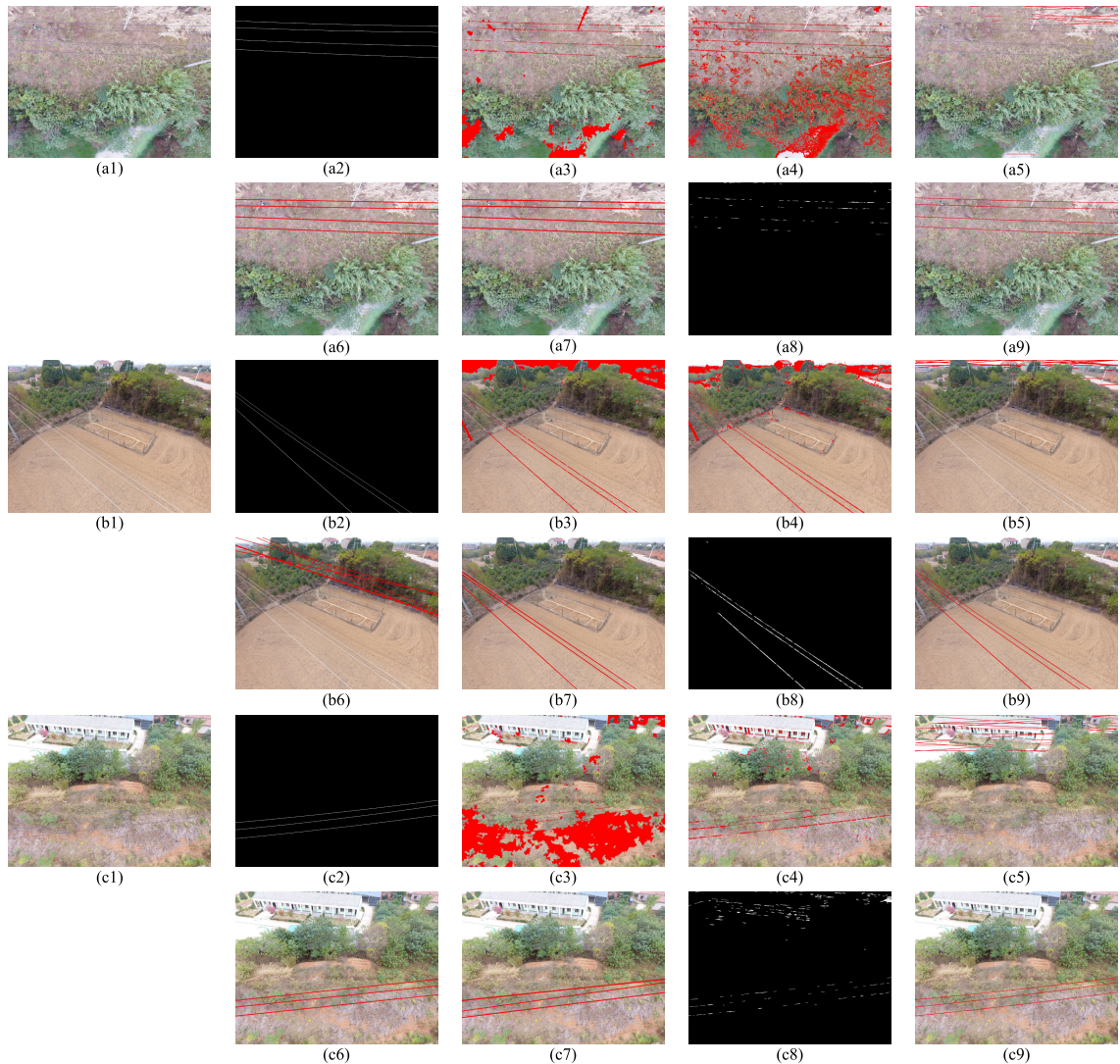


FIGURE 16. The experimental results of low IC images. (a1)(b1)(c1): the original image. The IC of three images are 32, 35 and 36, respectively; (a2)(b2)(c2): the ground truth; (a3)(b3)(c3): results of LSD-based OMRF method; (a4)(b4)(c4): results of LSD-based pMRF method; (a5)(b5)(c5): results of the TAPLD method; (a6)(b6)(c6): results of the AEPL method; (a7)(b7)(c7): results of the CRT method; (a8)(b8)(c8): temporary results of proposed method without EPF method; (a9)(b9)(c9): final label results of proposed method. Parameter k take value of 4, 4 and 5, respectively; Parameter β take value of 5, 4 and 5, respectively.

based on the pixels of entire image. Meanwhile, the TPR and FPR calculation results of all experimental data are shown in Table 2. The EF in Table 2 refers to the complete failure of power line extraction.

From the experimental results, it is known that both the LSD-based OMRF method and the LSD-based pMRF method will introduce a large amount of background noise, although they can connect part of power line segments. At the same time, the experimental results of LSD-based OMRF method are better than the experimental results of LSD-based pMRF method, because feature vectors in the LSD-based OMRF are object-level which not only increase the consistency of the power line regions but also reduce the influence of noise points compared to the features of a single pixel point. Therefore, the experimental results of LSD-based

OMRF method have higher TPR than the experimental results of LSD-based pMRF method overall. In addition, from the experimental results, the IC may have no effect on the above two methods. The similarities and differences between the spectral features of the non-power line region and the power line region, and their spatial neighborhood relationship are the key factors affecting the values of TPR and FPR.

For the TAPLD method and AEPL method, we can see that their performances are greatly influenced by prior knowledge based on the experiment results. The TAPLD method introduces a prior knowledge that the power lines have higher light reflectance and are brighter than the background. Therefore, when the pulse coupled neural filter(PCNF) is employed to detect edges and remove the background noise, the I component of the HSI space is used as the feeding input.

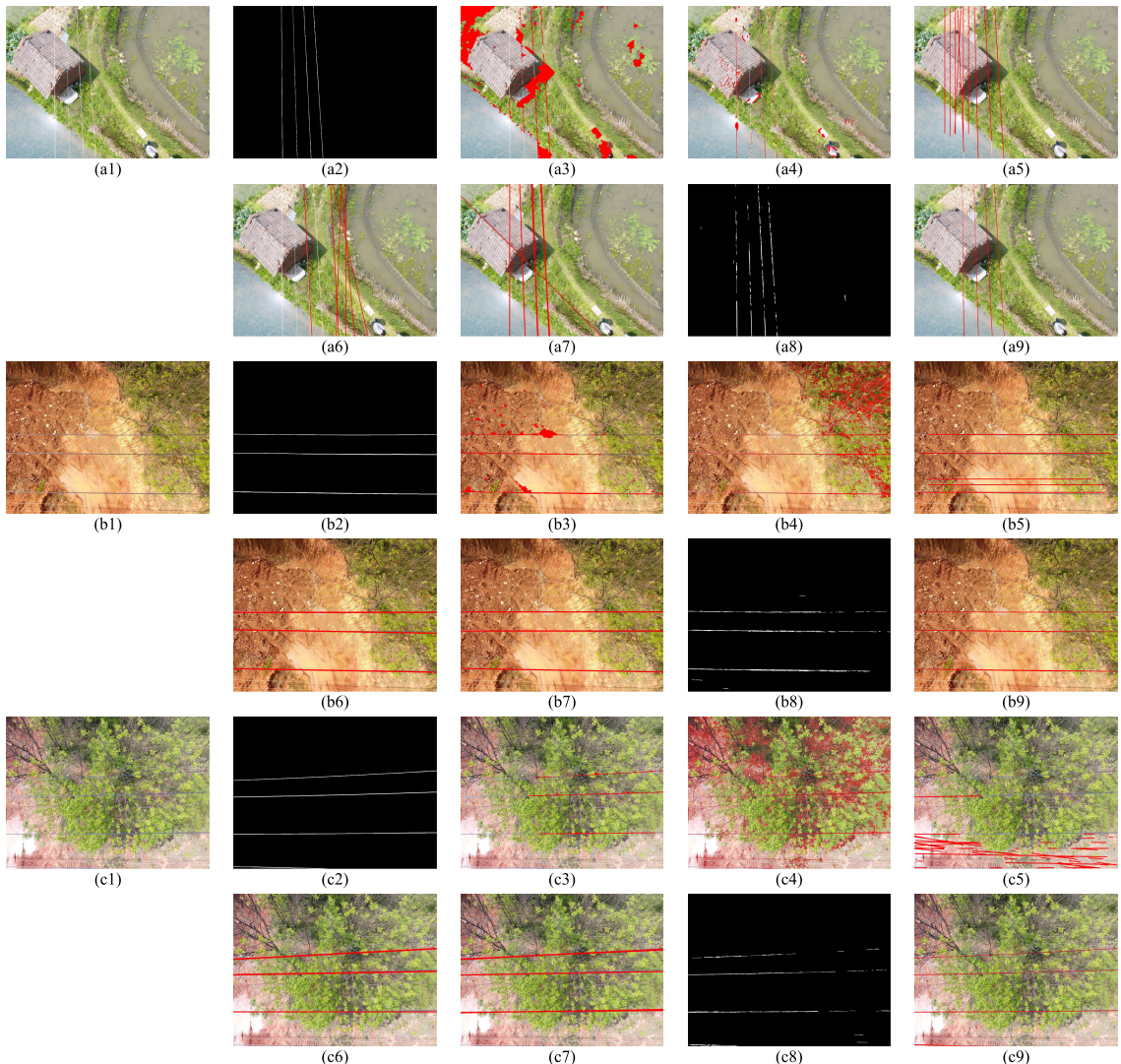


FIGURE 17. The experimental results of medium IC images. (a1)(b1)(c1): the original image. The IC of three images are 37, 38 and 41, respectively; (a2)(b2)(c2): the ground truth; (a3)(b3)(c3):results of LSD-based OMRF method; (a4)(b4)(c4): results of LSD-based pMRF method; (a5)(b5)(c5): results of the TAPLD method; (a6)(b6)(c6): results of the AEPL method; (a7)(b7)(c7): results of the CRT method; (a8)(b8)(c8): temporary results of proposed method without EPF method; (a9)(b9)(c9): final label results of proposed method. Parameter k take value of 7, 6 and 7, respectively. Parameter β take value of 4, 10 and 10, respectively.

However, the environment of power line corridor is complicated, and the brightness of the power lines are influenced by their material and external light. It is difficult to guarantee that the brightness of power lines in different scenes must be higher than the background. And even the brightness of the same power line is not exactly consistent at different positions. As shown in Fig.16(a5), Fig.16(b5), Fig.16(c5) and Fig.18(c5), the TAPLD method fails to detect the power lines at all because there are some background regions in the image that are brighter than the power lines and the pixels of these regions are pulsed before the pixels of power lines in the iterative process of PCNF. As shown in Fig.17(a5), Fig.17(b5), Fig.18(a5) and Fig.18(b5), when the power lines are brighter than most of the background region, the TAPLD method has obtained relatively good experimental results.

However, in the case of noise filtering using Kmeans in the Hough space, only a single angle feature is considered, so the non-power line segments whose angles are similar to the power lines are also determined as power lines, which cause an increase of FPR. For the AEPL method, a prior knowledge that the power line has a lower reflectance than its surrounding background which is completely opposite to the TAPLD method is given in reference [17]. The contradiction of this prior knowledge is caused by the difference in the flying height, weather conditions and power line material types when using the UAVs to collect aerial images. Based on this prior knowledge, the constraint that the mean intensities of the pixels in the two side sub-windows are greater than the mean intensity of the pixels in the middle sub-window is added when the ratio line detetor is employed to detect

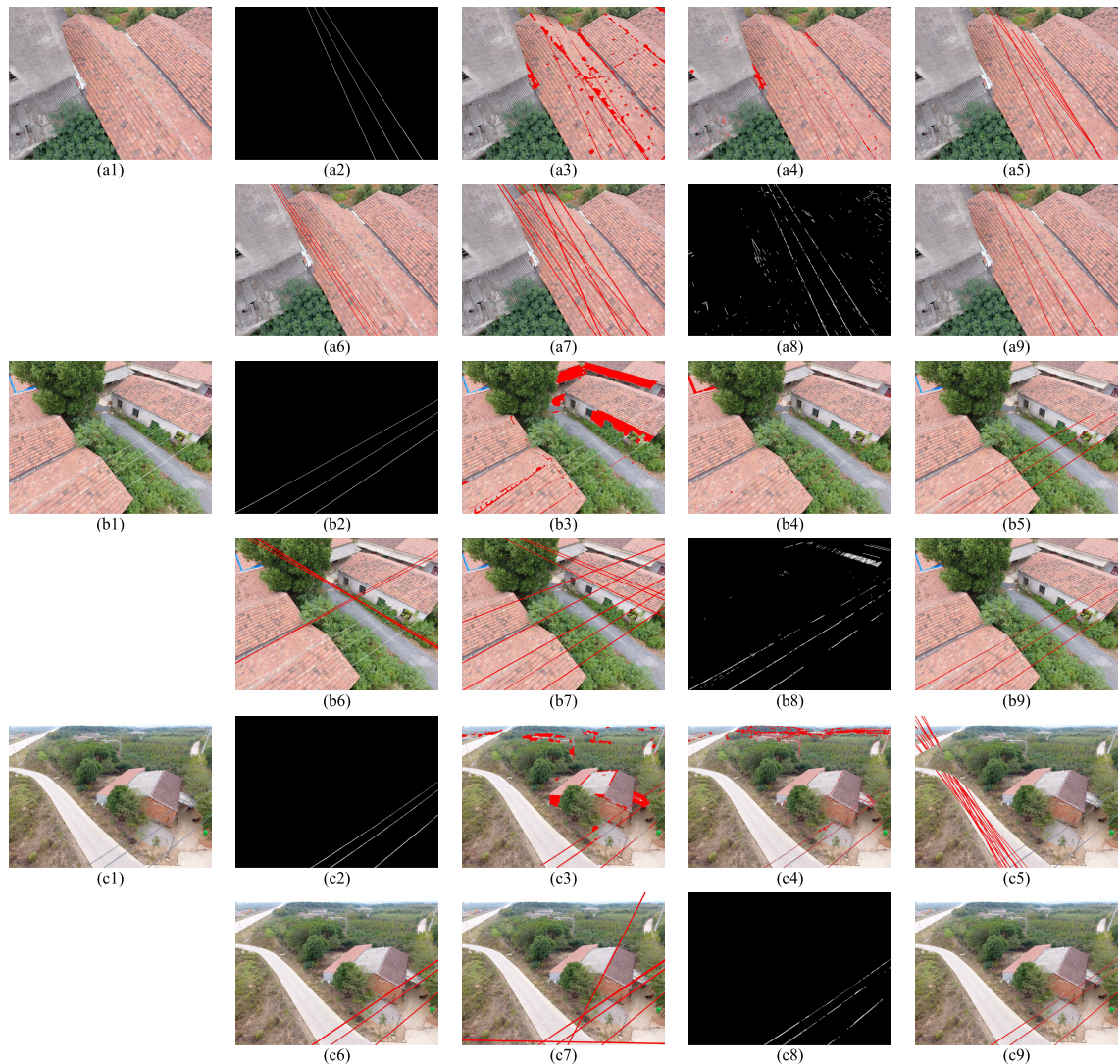


FIGURE 18. The experimental results of high IC images. (a1)(b1)(c1): the original image. The IC of three images are 42, 43 and 46, respectively; (a2)(b2)(c2): the ground truth; (a3)(b3)(c3): results of LSD-based OMRF method; (a4)(b4)(c4): results of LSD-based pMRF method; (a5)(b5)(c5): results of the TAPLD method; (a6)(b6)(c6): results of the AEPL method; (a7)(b7)(c7): results of the CRT method; (a8)(b8)(c8): temporary results of proposed method without EPF method; (a9)(b9)(c9): final label results of proposed method. Parameter k take value of 9, 9 and 10, respectively. Parameter β take value of 5, 13 and 8, respectively.

lines. As shown in Fig.16(b6), Fig.17(a6), Fig.18(a6) and Fig.18(b6), when the prior knowledge does not match the experimental data, as with the TAPLD method, the same detection failure condition occurs in the AEPL method. As shown in Fig.16(a6), Fig.16(c6), Fig.17(b6), Fig.17(c6) and Fig.18(c6), when the prior knowledge conforms to the actual situation, the AEPL method also achieved relatively good results. However, when the ratio line detector is used to detect lines, the non-power line edges with lower brightness are also retained in the edge map and there are some non-power line segments in the result of the Radon transform. Therefore, it is possibility that the detected power lines may deviate from the real power lines positions because the line grouping algorithm does not have an effective noise filtering function. Furthermore, from the experimental results, we can

see that the performances of the two methods are independent of the IC but more depends on the degree of matching between the experimental data and the prior knowledge.

For the CRT method, it mainly has two limitations. (1) It can not distinguish between power lines and non-power lines effectively for some scenes. (2) The results of power line extraction deviate from the real orientation of the power lines. The main reason of the first limitation is that the criterion for distinguishing between power lines and non-power lines is not reliable enough. On the one hand, the background on both sides of the non-power line may be similar. As shown in Fig.18(a7) and Fig.18(b7), although the background on both sides of the power line is almost identical, some non-power lines, such as the linear edges of the roof, also conform to the power line selection rules. On the

TABLE 2. Power line extraction performance with comparison methods.

Scenes	LSD+OMRF [36], [43]		LSD+pMRF [34], [43]		TAPLD [9]		AEPL [17]		CRT [24]		Proposed	
	TPR	FPR	TPR	FPR	TPR	FPR	TPR	FPR	TPR	FPR	TPR	FPR
Fig.16(a1)	0.7584	0.0545	0.6166	0.1497	EF*	0.0083	0.6528	0.0166	0.6861	0.0222	0.8331	0.0060
Fig.16(b1)	0.8156	0.0689	0.4881	0.0488	EF*	0.0171	EF*	0.0214	0.7795	0.0114	0.9472	0.0072
Fig.16(c1)	0.6496	0.1988	0.5922	0.0205	EF*	0.0184	0.5060	0.0125	0.5820	0.0159	0.8959	0.0045
Fig.17(a1)	0.6030	0.0742	0.5703	0.0079	0.7888	0.0215	0.1076	0.0176	0.8476	0.0205	0.9263	0.0021
Fig.17(b1)	0.6682	0.0137	0.5819	0.0577	0.2773	0.0193	0.7642	0.0168	0.8289	0.0135	0.9306	0.0030
Fig.17(c1)	0.4924	0.0022	0.5583	0.1083	0.1758	0.0333	0.6283	0.0187	0.6206	0.0211	0.8029	0.0015
Fig.18(a1)	0.8806	0.0370	0.7481	0.0106	0.8693	0.0140	0.0125	0.0097	0.9336	0.0307	0.9637	0.0039
Fig.18(b1)	0.3881	0.0585	0.3361	0.0057	0.8052	0.0049	0.0115	0.0243	0.8396	0.0362	0.9564	0.0042
Fig.18(c1)	0.7774	0.0301	0.5499	0.0247	0.0341	0.0304	0.8067	0.0087	0.8172	0.0262	0.8610	0.0022

* : The EF in Table 2 is an abbreviation for extraction failure.

other hand, the background on both sides of some power lines may be obviously different. For example, as shown in Fig.17(a7) and Fig.18(c7), there is a house or plant in the background on one side of the power line, and no such object in the background on the other side. In this case, in order to obtain complete power lines, the evaluation criteria for the similarity of background must be lowered, so that some non-power lines cannot be filtered out. For the second limitation of CRT method, it is mainly because that the power line may have a slight curvature. The CRT method only regards the power lines as standard straight lines and does not use any fitting algorithm. As shown in the Fig.16(a7), Fig.16(b7), Fig.16(c7), Fig.17(b7) and Fig.17(c7), although no non-power lines are wrongly divided into the power line class, the orientation of the extracted power lines deviate from the actual orientation of power lines. Therefore, the experimental results of the CRT have lower TPR and higher FPR than the method proposed in this paper due to the above two limitations. In addition, as shown in Table.2, the performance of the CRT method is not related to the *IC*, and it depends on the curvature of power lines and the background distribution in the aerial images.

As shown in Fig.16-Fig.18 and Table 2, the proposed method has better performance than the other 5 methods, with higher TPR and lower FPR. The superiority of the proposed method is mainly reflected in the following three aspects. Firstly, in the line detection step, the LSD method is used to extract all the line segments in the image without introducing any prior knowledge to filter out the power line segments. Although there will be a large number of non-power line segments in the line segment candidate pool, it still retains the greatest extent information of power line. Moreover, at the classification step, the OMRF-AWP method can not only divide the power line segments into one class as much as possible, but also not divide the background noise outside the line segment candidate pool into the power line class. Because compared with the other five methods, it adopts

multi-dimensional features, considering not only the spectral information, but also the gradient angle change and regional consistency. Compared with the other two MRF-based methods, the proposed method only considers the classification of LSD extraction results, so it does not introduce a lot of background noise. In the label field modeling process, the original isotropic model is transformed into an angle-based anisotropy model that is more confirm to the actual situation of power line detection. So the regions which are spatially adjacent and angularly similar can be scored as much as possible. Meanwhile, as shown in Fig.16(a8), Fig.16(b8), Fig.16(c8), Fig.17(a8), Fig.17(b8), Fig.17(c8), Fig.18(a8), Fig.18(b8) and Fig.18(c8), compared with LSD-based OMRF method and LSD-based pMRF method, although the power line segments are disconnected from each other, there are fewer FP in the power line extraction result which obtained by the OMRF-AWP method. Finally, based on EPF method, we can not only group the power line segments accurately and filter out the remaining non-power line segments, but also fit the power lines accurately as much as possible. In addition, as shown in Table 2, although the *IC* has an effect on the setting of parameter *k*, it does not directly determine the final power line extraction accuracy. Because even if the TPR of the power line extraction result of the low *IC* image acquired by the OMRF-AWP method is higher than the TPR of the extraction result of high *IC* image, the distribution of the power line segments may be nonuniform, which leads to the inaccuracy of the envelopes, and the TPR of the final experimental result of low *IC* image may be lower than high *IC* image.

D. METHOD VALIDATION IN SPECIAL SCENES

The proposed method is to extract the power lines from the aerial images of the UAVs with complex background. The experiments in the previous section have demonstrated the applicability of the proposed method and its superiority over some other methods in several general scenes.

TABLE 3. Power line extraction performance in special complex scenes.

Categories	Scenes	TPR	FPR
Complex Distribution	Fig.20(a1)	0.9579	0.0037
	Fig.20(b1)	0.8541	0.0057
Different Resolutions	Fig.21(a1)	0.9208	0.0016
	Fig.21(b1)	0.9530	0.0014
	Fig.21(c1)	0.8569	0.0013
	Fig.21(d1)	0.6636	0.0043
Electric Tower	Fig.23(a1)	0.8814	0.0025
	Fig.23(b1)	0.8207	0.0027
	Fig.23(c1)	0.8557	0.0066
	Fig.23(d1)	0.8384	0.0071

In this section, we will verify the effectiveness of the proposed method in extracting power lines for some special complex scenes. The experimental content is mainly composed of the following aspects: case that the power lines are partially obscured in the image, case that power lines have complex distribution, case that aerial images have different spatial resolutions, and case that the electric tower and the power line coexist.

As shown in Table 3, the evaluation indicators of the power line extraction results still use TPR and FPR. Specifically, as shown in Fig.19(a1), Fig.19(b1), Fig.19(c1), and Fig.20(c1), for the case that power lines are partially obscured, we can't give real manual labeling, so we don't provide the TPR and FPR for these scenes.

1) BLOCKING CASE

In this subsection, we mainly discuss the performance of the proposed method in dealing with blocking case. As shown in Fig.19(a1), Fig.19(b1) and Fig.19(c1), power lines are partially obscured by leaves or branches. In essence, the influence of the obstructions on the proposed method is mainly reflected in the following two aspects: (1) When the line segment candidate pool is established by utilizing the LSD method, the obstructions may increase the interference line segment regions near the power lines. (2) In the line segment candidate pool, the obscured power line portion cannot be extracted by the LSD method, which increases break length of power lines. First, as shown in Fig.19(a2), Fig.19(b2) and Fig.19(c2), the former problem can be effectively solved because that the OMRF-AWP method proposed in this paper has a strong ability to distinguish between power lines and non-power lines. Second, as shown in Fig.19(a3), Fig.19(b3) and Fig.19(c3), the EPF method proposed in this paper can effectively solve the problem that the structure of power line is discontinuous.

However, the following two situations may reduce the accuracy of our method. (1) If the power lines are obscured by a large area, the power line segments in the line segment



FIGURE 19. The experimental results of blocking case. (a1)(b1)(c1): the original images; (a2)(b2)(c2): temporary results of proposed method without EPF method; (a3)(b3)(c3):final label results of proposed method.

candidate pool are few and the distance between them is large, the power line fitting results based on the EPF method may deviate from the actual orientation. (2) If the spectrum and angle features of the linear structure of the obstructions are very similar to their surrounding power lines, they may be misclassified into the power line class, which may reduce the accuracy in the subsequent fitting process of the power line segments by the EPF method.

2) COMPLEX DISTRIBUTION OF POWER LINES

In this subsection, we mainly discuss the performance of the proposed method in dealing with the scenes that power lines have complex distribution. As shown in Fig.20(a1), Fig.20(b1) and Fig.20(c1), the power lines are composed of upper and lower power lines, and the power lines of each layer have different directions. When the power line segments are extracted from the line segment candidate pool based on OMRF-AWP method, the power lines of the upper and lower layers will be divided into two classes. This is because the OMRF-AWP method uses a potential function with anisotropic weighted penalty when calculating the probability of the label field implementation, so the probability of dividing the line segment regions with similar angles into one class is increased. Then we can use the EPF method to fit the power line segments in the two classes and merge the results.

As shown in Fig.20(a2), Fig.20(a3), Fig.20(b2), Fig.20(b3), Fig.20(c2) and Fig.20(c3), the upper and lower power lines are successfully divided into two classes. In Fig.20(a2) and Fig.20(a3), the power lines in the two classes obtained by OMRF-AWP method are relatively complete and pure. Compared with Fig.20(a1), the background of Fig.20(b1) is more complex and the signal of the lower power lines is pretty weak. Therefore, as shown in Fig.20(b2) and Fig.20(b3), the power lines classification result of the lower power line is worse than that of the upper layer, which results in the situation that the fitting result of lower power lines deviate

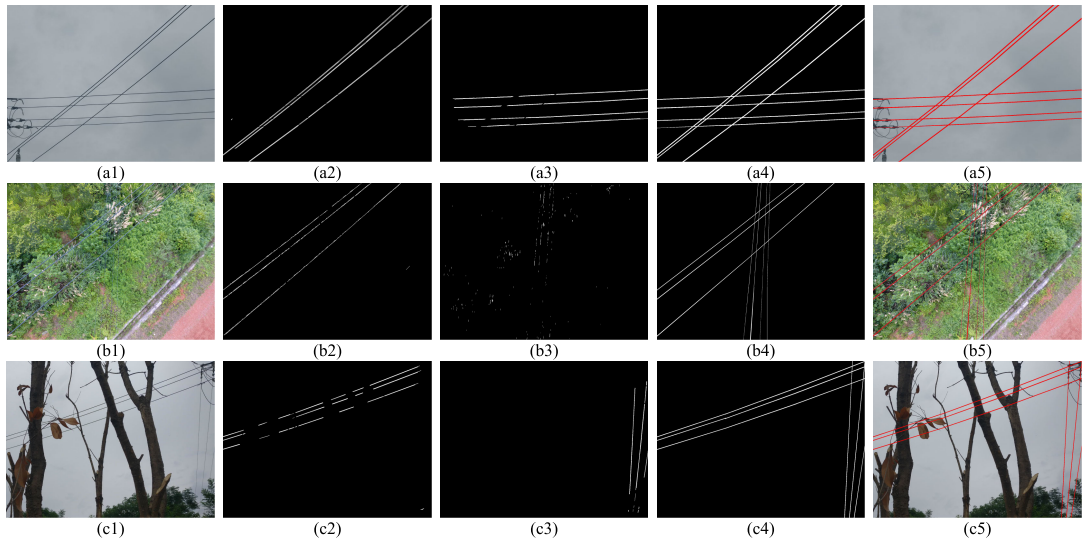


FIGURE 20. The experimental results of scenes that power lines have complex distribution. (a1)(b1)(c1): the original images; (a2)(a3)(b2)(b3)(c2)(c3): temporary results of proposed method without EPF method; (a4)(b4)(c4): fitting fusion results for each class based on EPF method; (a5)(b5)(c5): final label results of proposed method. .

from the actual orientation of power lines. The power line in Fig.20(c3) has not only a two-layer structure, but also the power lines of each layer are partially obscured. As shown in Fig.20(c2)-(c5), the proposed method still achieves good performance.

3) DIFFERENT SPATIAL RESOLUTIONS

The use of UAVs for power line inspection is becoming a trend, as the imaging technology of cameras carried by UAVs is becoming more advanced and the resolution is getting higher and higher. Also because UAVs can be very close to the power lines, the subtle problems in the power corridor can be found. All in all, the aerial images taken during the UAVs missions are mostly close-up, high-resolution images. However, when UAV is used for power line inspection, the spatial resolution of the images obtained is different because of the shooting height. In order to verify the performance of the method at different resolutions, we select a power line scene and get different resolutions by adjusting the UAV height, and use the proposed method to extract power lines. The experimental results are shown in the Fig.21. The TPR and FPR are shown in Table 3.

As shown in the Fig.21, (a1), (b1), (c1), and (d1) are the same scene of different heights, and the spatial resolutions are $0.0113*0.0112\text{ m}^2$, $0.0142*0.0139\text{ m}^2$, $0.0170*0.0167\text{ m}^2$, and $0.0198*0.0195\text{ m}^2$, respectively. Among them, Fig.21(a1) and Fig.21(b1) have lower shooting heights, while Fig.21(c1) and Fig.21(d1) have higher shooting heights. It can be seen that when the resolution is high, the power line classification result and the fitting result are better. However, when the resolution is low, such as Fig.21(d1), the extraction result of the power line deviates from the real orientation.



FIGURE 21. The experimental results of the images with different resolutions. (a1)(b1)(c1)(d1): the original images; (a2)(b2)(c2)(d2): temporary results of proposed method without EPF method; (a3)(b3)(c3)(d3): final label results of proposed method. .

As the shooting height increases, the resolution decreases and the power line portion of the scene blurs due to the camera sampling mechanism. The difference between the power line and the scenes on both sides decreases which causes the linear regions extracted by the LSD method to be gradually reduced. In the classification process, with these extracted linear regions as the whole, the part of the power line obtained by the classifier also decrease, which causes

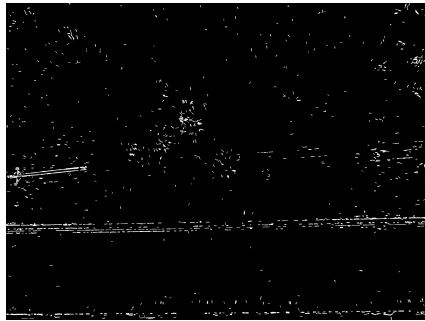


FIGURE 22. Line segments extraction result of Fig.21(d1) based on LSD method.

the fitting process to be deviated. For Fig.21(d1) which has a lower resolution, the power line portion on the left is substantially undetected during the extraction phase of the linear regions as shown in Fig.22. Therefore, the power line portion of the classification result contains only a few areas on the right side, which causes a deviation of the left power line.

4) INFLUENCE OF ELECTRIC TOWER

The electric tower is an important part of the power line corridor. In this subsection, we will verify the impact for our proposed method when the tower appears in the aerial images. The target of the tower in the aerial image is obvious and has linear features. It is easy to extract many linear regions by the LSD method and the directions of extracted tower regions are confusing. Some tower's linear regions may have same direction and similar spectral feature with the extracted power line regions, and they are close in space. This causes that some linear regions of the tower may be classified into the power line class. The power lines on both sides of the tower form a large angle because of the sag phenomenon. Although the power lines on both sides can be classified into one class during the classify process, the fitted power line will deviate from the real power line because of the angle difference of the power lines on both sides of the tower. For example, the second and third fitted power lines results on the upper right of Fig.23(c3) fail to coincide with the real power lines on the right side of the tower. The two fitted power lines results on the right side of the Fig.23(d3) are off the real power line on the right side of the tower. Therefore, when the tower appears in the aerial image, the classification process of the proposed method performs well, but the fitting process may be deviated due to the angle between the power lines on both sides. However, if the UAVs can fly stably to the top of the tower for the overhead shot, the impact of the fitting may be reduced, and the fitting accuracy can be improved.

E. DISCUSSION

In this section, we further discuss the advantages and limitations of the proposed method. In summary, there are two main advantages of the proposed method: On the one hand, the result of power line extraction is accurate with a higher TPR and a lower FPR in comparison with several existing

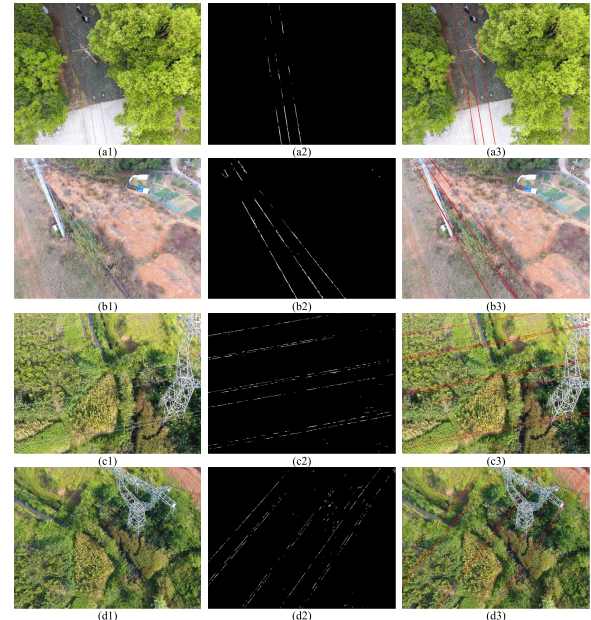


FIGURE 23. The experimental results of scenes where the electric tower and the power line coexist.(a1)(b1)(c1)(d1): the original images; (a2)(b2)(c2)(d2): temporary results of proposed method without EPF method;(a3)(b3)(c3)(d3): final label results of proposed method.

methods. On the other hand, the proposed method has stable performance in some complex scenes, e.g., some special cases, such as blocking case. The reasons for the above advantages are shown as follows:

(1) When constructing the line segment candidate pool, we choose the LSD method which is sensitive to linear edges, so that we can retain as many linear segment regions belonging to the power line in the image as possible. In this way, although the workload is large in the subsequent classification process, more power line segments can be obtained at the classification process, and the TPR is maintained at a high level. In the AEPL method and the TAPLD method, when linear segment regions are extracted, in order to alleviate the computational pressure of distinguishing between power lines and non-power lines in the subsequent classification process, they all use prior knowledge to achieve initial filtering of non-power lines. It is unreasonable because the power line target in the aerial image is weak. If the prior knowledge is used overmuch in the process of extracting the line segment regions, it is often easy to miss the power line segments. Moreover, once the prior knowledge is wrong or the prior knowledge and the image scene do not match, the result of the power line extraction will be incomplete and the TPR will be low.

(2) In this paper, the OMRF-AWP method is faced with all line segment regions in the candidate pool. The line segment regions in the candidate pool are spatially non-adjacent and the network topology constructed by the line segment regions in the candidate pool has no regularity. Therefore, when describing the spatial relationship, this paper adopts the idea of K-Nearest Neighbor. The nearest K regions

are used as neighborhood elements, which solves the topological relationship of non-adjacent spaces between nodes. Meanwhile, we define the label field model with anisotropic weighted penalty which can optimize classification results by angle difference between power lines and other line segments. For the LSD-based pMRF method and LSD-based OMRF method, when distinguishing between power lines and non-power lines, they are more affected by background noise because only isotropic spatial contextual relationships are considered when modeling the label field. For AEPL method, TAPLD method, CRT method, their abilities to distinguish between power lines and non-power lines depend on the suitability between the image scenes and the prior knowledge, which is easy to cause misclassification, resulting in a higher FPR value for the final classification. Therefore, the results obtained by the proposed method have lower FPR values.

(3) Compared with CRT method, AEPL method and TAPLD method, the EPF method take the situation that the power lines have a slight curvature and a certain width into account when grouping and connecting power line segments. In the fitting step, we use a piecewise envelope fitting method with overlapping regions. After considering the overlaps, the fitting problem in the scene of slight curvature of power lines can be effectively solved, and the envelope-based fitting process can take the width of the power line into account during the final fitting stage. It can ensure the accuracy of power line fitting process as much as possible. Therefore, the proposed method have higher TPR and lower FPR.

(4) The classification capabilities of OMRF-AWP method is excellent, which can accurately distinguish between power lines and non-power lines, even if there are many non-power line segment regions in the line segment candidate pool. The OMRF-AWP method not only considers the local features of the power lines, but also considers the contextual spatial relationship of the line segment regions combined with the line segment region angle from a macro perspective. By combining the local and overall information, the class of the linear segments is determined. Moreover, OMRF-AWP method is an unsupervised method and does not need prior knowledge, which uses the generator method to describe the distribution function of the power line itself. In the modeling process of the feature field, the Gaussian mixture model is adopted, which conforms to the natural distribution law. At the same time, combined with the Bayesian formula and the MAP criterion, the rationality of the segmentation result can be further verified. Hence, the OMRF-AWP method has a stable ability to distinguish between power line segments and non-power line segments in a variety of scenes. Meanwhile, the EPF method proposed in this paper can effectively cluster and fit the power line segments obtained by OMRF-AWP method, which can ensure the continuity and completeness of the power lines. Therefore, the method in this paper is stable and workable in many scenes.

However, the proposed method in this paper also has shortcomings and needs further research. Such as:

(1) The modeling process of the OMRF-AWP method based on probability analysis is slightly complicated. In order to better fit the distribution and expression information of the power line image, the feature random field and the label random field are constructed according to feature and spatial information respectively when constructing the model, and the MAP criterion is used in the update iteration. Therefore, the whole modeling process is more complicated.

(2) Parameters involved in the OMRF-AWP method cannot be adaptive. The MRF-based methods need to set parameters of the potential energy function β and the number of classifications k . Although we have explained their setup strategy in detail in Section IV-B, they are not adaptive.

V. CONCLUSION

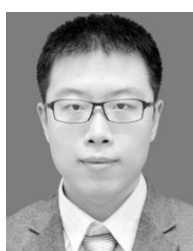
In this paper, the novel OMRF-AWP method and EPF method have been proposed, by which power lines can be extracted accurately from the aerial images with complex background. In the OMFR-AWP method, we have defined a new neighborhood system based on the irregular graph model and built an anisotropic MLL model with weighted penalty, by which power line segments can be accurately extracted from the line segment candidate pool without any prior knowledge or auxiliary information. Meanwhile, the EPF method can not only fit the power line accurately, but also further filter out the non-power line segments that are misclassified into the power line class. The validity of the proposed method is proved by qualitatively and quantitatively analysis of the experimental results.

In future research, we expect to conduct more in-depth research in the following aspects: (1) We would like to consider how to convert the parameter setting of the proposed method to adaptive mode and reduce manual intervention; (2) We want to select a more suitable feature field distribution function; (3) We would like to investigate whether there is a classifier that replaces MRF; (4) We would like to do the extraction of other components in the power line corridor, such as insulator, pylon, etc.

REFERENCES

- [1] J. Katrasnik, F. Pernus, and B. Likar, "A survey of mobile robots for distribution power line inspection," *IEEE Trans. Power Del.*, vol. 25, no. 1, pp. 485–493, Jan. 2010.
- [2] N. Pouliot, P.-L. Richard, and S. Montambault, "LineScout technology opens the way to robotic inspection and maintenance of high-voltage power lines," *IEEE Power Energy Technol. Syst. J.*, vol. 2, no. 1, pp. 1–11, Mar. 2015.
- [3] Van N. Nguyen, R. Jenssen, and D. Roverso, "Automatic autonomous vision-based power line inspection: A review of current status and the potential role of deep learning," *Int. J. Electr. Power Energy Syst.*, vol. 99, pp. 107–120, Jul. 2017.
- [4] L. Matikainen, M. Lehtomäki, E. Ahokas, J. Hyppä, M. Karjalainen, and A. Jaakkola, "Remote sensing methods for power line corridor surveys," *ISPRS J. Photogramm. Remote Sens.*, vol. 119, pp. 10–31, Sep. 2016.
- [5] J. Ahmad, A. S. Malik, L. Xia, and N. Ashikin, "Vegetation encroachment monitoring for transmission lines right-of-ways: A survey," *Electr. Power Syst. Res.*, vol. 95, no. 1, pp. 339–352, Feb. 2013.
- [6] J. A. J. Berni, P. J. Zarco-Tejada, L. Suarez, and E. Fereres, "Thermal and narrowband multispectral remote sensing for vegetation monitoring from an unmanned aerial vehicle," *IEEE Trans. Geosci. Remote Sens.*, vol. 47, no. 3, pp. 722–738, Mar. 2009.

- [7] Z. Zhou, C. Zhang, C. Xu, F. Xiong, Y. Zhang, and T. Umer, "Energy-efficient industrial Internet of UAVs for power line inspection in smart grid," *IEEE Trans. Ind. Inform.*, vol. 14, no. 6, pp. 2705–2714, Jun. 2018.
- [8] H. Shan, J. Zhang, X. Cao, X. Li, and D. Wu, "Multiple auxiliaries assisted airborne power line detection," *IEEE Trans. Ind. Electron.*, vol. 64, no. 6, pp. 4810–4819, Jun. 2017.
- [9] Z. Li, Y. Liu, R. Walker, R. Hayward, and J. Zhang, "Towards automatic power line detection for a UAV surveillance system using pulse coupled neural filter and an improved Hough transform," *Mach. Vis. Appl.*, vol. 21, no. 5, pp. 677–686, Aug. 2010.
- [10] R. A. McLaughlin, "Extracting transmission lines from airborne LIDAR data," *IEEE Geosci. Remote Sens. Lett.*, vol. 3, no. 2, pp. 222–226, Apr. 2006.
- [11] S. Deng, P. Li, J. Zhang, and J. Yang, "Power line detection from synthetic aperture radar imagery using coherence of co-polarisation and cross-polarisation estimated in the Hough domain," *IET Radar, Sonar Navigat.*, vol. 6, no. 9, pp. 873–880, Dec. 2012.
- [12] K. Sarabandi and M. Park, "Extraction of power line maps from millimeter-wave polarimetric SAR images," *IEEE Trans. Antennas Propag.*, vol. 48, no. 12, pp. 1802–1809, Dec. 2000.
- [13] F. Tian, Y. Wang, and L. Zhu, "Power line recognition and tracking method for UAVs inspection," in *Proc. IEEE Int. Conf. Inf. Automat. (ICIA)*, Aug. 2015, pp. 2136–2141.
- [14] B. Song and X. Li, "Power line detection from optical images," *Neurocomputing*, vol. 129, pp. 350–361, Apr. 2014.
- [15] C. Shuai, H. Wang, G. Zhang, Z. Kou, and W. Zhang, "Power lines extraction and distance measurement from binocular aerial images for power lines inspection using UAV," in *Proc. 9th Int. Conf. Intell. Hum.-Mach. Syst. Cybern. (IHMSC)*, Aug. 2017, pp. 69–74.
- [16] T. Yang, H. Yin, Q. Q. Ruan, J. D. Han, J. T. Qi, Q. Yong, Z. T. Wang, and Z. Q. Sun, "Overhead power line detection from uav video images," in *Proc. IEEE 19th Int. Conf. Mechatronics Mach. Visi. Prac. (M2VIP)*, Nov. 2012, pp. 74–79.
- [17] G. Yan, C. Li, G. Zhou, W. Zhang, and X. Li, "Automatic extraction of power lines from aerial images," *IEEE Geosci. Remote Sens. Lett.*, vol. 4, no. 3, pp. 387–391, Jul. 2007.
- [18] Z. Li, Y. Liu, R. Hayward, J. Zhang, and J. Cai, "Knowledge-based power line detection for uav surveillance and inspection systems," in *Proc. IEEE 23th Int. Conf. Image Vis. Comput. New Zealand (IVCNZ)*, Nov. 2008, pp. 1–6.
- [19] I. Golightly and D. Jones, "Corner detection and matching for visual tracking during power line inspection," *Image Vis. Comput.*, vol. 21, no. 9, pp. 827–840, Sep. 2003.
- [20] J. Zhang, H. Shan, X. Cao, P. Yan, and X. Li, "Pylon line spatial correlation assisted transmission line detection," *IEEE Trans. Aerosp. Electron. Syst.*, vol. 50, no. 4, pp. 2890–2905, Oct. 2014.
- [21] X. Liu, L. Hou, and X. Ju, "A method for detecting power lines in UAV aerial images," in *Proc. IEEE 3th Int. Conf. Comput. Commun. (ICCC)*, Dec. 2017, pp. 2132–2136.
- [22] W. Cao, X. Yang, L. Zhu, J. Han, and T. Wang, "Power line detection based on symmetric partial derivative distribution prior," in *Proc. IEEE Int. Conf. Inform. Autom. (ICIA)*, Aug. 2013, pp. 767–772.
- [23] J. Zhang, L. Liu, B. Wang, X. Chen, Q. Wang, and T. Zheng, "High speed automatic power line detection and tracking for a UAV-based inspection," in *Proc. IEEE Int. Conf. Ind. Control Electron. Eng. (ICICEE)*, Aug. 2012, pp. 266–269.
- [24] Y. Chen, Y. Li, H. Zhang, L. Tong, Y. Cao, and Z. Xue, "Automatic power line extraction from high resolution remote sensing imagery based on an improved radon transform," *Pattern Recognit.*, vol. 49, pp. 174–186, Jan. 2016.
- [25] Z. Chen, Y. Zhang, and L. Wang, "Semantic segmentation of remote sensing imagery using an object-based Markov random field model with auxiliary label fields," *IEEE Trans. Geosci. Remote Sens.*, vol. 55, no. 5, pp. 3015–3028, May 2017.
- [26] M. Ciechowski, "Automated coronal hole segmentation from solar EUV Images using the watershed transform," *J. Vis. Communun. Image Represent.*, vol. 33, pp. 203–218, Nov. 2015.
- [27] J. Cousty, G. Bertrand, L. Najman, and M. Couprise, "Watershed cuts: Thinnings, shortest path forests, and topological watersheds," *IEEE Trans. Pattern Anal. Mach. Intell.*, vol. 32, no. 5, pp. 925–939, May 2010.
- [28] D. Comaniciu and P. Meer, "Mean shift: A robust approach toward feature space analysis," *IEEE Trans. Pattern Anal. Mach. Intell.*, vol. 24, no. 5, pp. 603–619, May 2002.
- [29] J. Yang, Z. Gan, K. Li, and C. Hou, "Graph-based segmentation for RGB-D data using 3-D geometry enhanced superpixels," *IEEE Trans. Cybern.*, vol. 45, no. 5, pp. 927–940, May 2015.
- [30] D. Stutz, A. Hermans, and B. Leibe, "Superpixels: An evaluation of the state-of-the-art," *Comput. Vis. Image Underst.*, vol. 166, pp. 1–27, Jan. 2018.
- [31] M. Ciechowski and J. H. Spodnik, "Semi-automatic corpus callosum segmentation and 3d visualization using active contour methods," *Symmetry*, vol. 10, no. 11, p. 589, 2018.
- [32] K. Ding, L. Xiao, and G. Weng, "Active contours driven by local pre-fitting energy for fast image segmentation," *Pattern Recogn. Lett.*, vol. 104, no. 1, pp. 29–36, Mar. 2018.
- [33] L. Zhang and Q. Ji, "Image segmentation with a unified graphical model," *IEEE Trans. Pattern Anal. Mach. Intell.*, vol. 32, no. 8, pp. 1406–1425, Aug. 2010.
- [34] S. Geman and D. Geman, "Stochastic relaxation, Gibbs distributions, and the Bayesian restoration of images," *IEEE Trans. Pattern Anal. Mach. Intell.*, vol. PAMI-6, no. 6, pp. 721–741, Nov. 1984.
- [35] C. Zheng and H. Yao, "Segmentation for remote-sensing imagery using the object-based Gaussian–Markov random field model with region coefficients," *Int. J. Remote Sens.*, vol. 40, no. 11, pp. 4441–4472, 2019.
- [36] C. Zheng and L. Wang, "Semantic segmentation of remote sensing imagery using object-based Markov random field model with regional penalties," *IEEE J. Sel. Topics Appl. Earth Observ. Remote Sens.*, vol. 8, no. 5, pp. 1924–1935, May 2015.
- [37] Z. Xu, B.-S. Shin, and R. Klette, "Accurate and robust line segment extraction using minimum entropy with Hough transform," *IEEE Trans. Image Process.*, vol. 24, no. 3, pp. 813–822, Mar. 2015.
- [38] R. F. C. Guerreiro and P. M. Q. Aguiar, "Connectivity-enforcing Hough transform for the robust extraction of line segments," *IEEE Trans. Image Process.*, vol. 21, no. 12, pp. 4819–4829, Dec. 2012.
- [39] M. C. K. Yang, J.-S. Lee, C.-C. Lien, and C.-L. Huang, "Hough transform modified by line connectivity and line thickness," *IEEE Trans. Pattern Anal. Mach. Intell.*, vol. 19, no. 8, pp. 905–910, Aug. 1997.
- [40] L. Zheng and D. Shi, "Advanced radon transform using generalized interpolated Fourier method for straight line detection," *Comput. Vis. Image Understand.*, vol. 115, no. 2, pp. 152–160, Feb. 2011.
- [41] S. Daming, G. Junbin, P. S. Rahmdel, A. Michael, and C. Tony, "UND: Unite-and-divide method in Fourier and radon domains for line segment detection," *IEEE Trans. Image Process.*, vol. 22, no. 6, pp. 2500–2505, Jun. 2013.
- [42] N. Anantrasirichai, W. Hayes, M. Allinovi, D. Bull, and A. Achim, "Line detection as an inverse problem: Application to lung ultrasound imaging," *IEEE Trans. Med. Imag.*, vol. 36, no. 10, pp. 2045–2056, Oct. 2017.
- [43] R. G. von Gioi, J. Jakubowicz, J.-M. Morel, and G. Randall, "LSD: A fast line segment detector with a false detection control," *IEEE Trans. Pattern Anal. Mach. Intell.*, vol. 32, no. 4, pp. 722–732, Apr. 2010.
- [44] G. Tang, Z. Xiao, Q. Liu, and H. Liu, "A novel airport detection method via line segment classification and texture classification," *IEEE Geosci. Remote Sens. Lett.*, vol. 12, no. 12, pp. 2408–2412, Dec. 2015.
- [45] N. Liu, Z. Cui, Z. Cao, Y. Pi, and S. Dang, "Airport detection in large-scale SAR images via line segment grouping and saliency analysis," *IEEE Geosci. Remote Sens. Lett.*, vol. 15, no. 3, pp. 434–438, Mar. 2018.
- [46] Y. Li, Z. Hu, H. Gang, Z. Li, and M. A. Sotelo, "Image sequence matching using both holistic and local features for loop closure detection," *IEEE Access*, vol. 5, pp. 13835–13846, 2017.
- [47] X. Chen, C. Zheng, H. Yao, and B. Wang, "Image segmentation using a unified Markov random field model," *IET Image Process.*, vol. 11, no. 10, pp. 860–869, 2017.
- [48] J. Candamo, R. Kasturi, D. Goldgof, and S. Sarkar, "Detection of thin lines using low-quality video from low-altitude aircraft in urban settings," *IEEE Trans. Aerosp. Electron. Syst.*, vol. 45, no. 3, pp. 937–949, Jul. 2009.



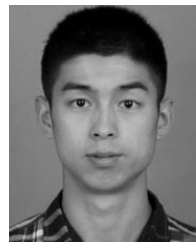
LE ZHAO received the B.S. and M.S. degrees from the Electronic Information School, Wuhan University, Wuhan, China, in 2014 and 2016, respectively, where he is currently pursuing the Ph.D. degree.

His research interests include computer vision, pattern recognition, and fault diagnosis of high voltage equipment.



XIANPEI WANG received the B.S. degree from North China Electric Power University, in 1984, and the M.S. and Ph.D. degrees from Wuhan University, in 1991 and 1999, respectively, where he is currently a Professor with the Electronic Information School.

He is the author/coauthor of over 50 articles in international and domestic journals. His research interests include computer vision, intelligent monitoring technique for power systems, systems reliability analysis, and fault diagnosis of high voltage equipment.



MENG TIAN (M'17) received the B.S. and Ph.D. degrees from the Electronic Information School, Wuhan University, Wuhan, China, in 2011 and 2016, respectively, where he is currently a Postdoctoral.

He is also a Visiting Scholar with Southern Methodist University. His research interests include security of cyber physical power systems and cascading failures of multilayer networks.



HONGTAI YAO received the B.S. degree from the School of Mathematics and Statistics, Zhengzhou University, Zhengzhou, China, in 2014, and the M.S. degree from the School of Mathematics and Statistics, Henan University, Kaifeng, in 2018. He is currently pursuing the Ph.D. degree with Wuhan University.

His research interests include remote sensing image segmentation and computer vision.



ZINI JIAN received the B.S. degree from the School of Information Science and Engineering, Wuhan University of Science and Technology, Wuhan, China, in 2015, and the M.S. degree from the College of Engineering and Computer Science, Syracuse University, Syracuse, USA, in 2017. She is currently pursuing the Ph.D. degree with Wuhan University.

Her research interests include medical image processing and security of cyber physical power systems.

• • •